7-9-2004

# Australian Great Barrier Reef Initiation Timing Constrained by Seaward Shallow-Water Sediment Drift Architecture (ODP Leg 194, Marion Plateau)

Stephen P. Obrochta
*University of South Florida*

# Australian Great Barrier Reef Initiation Timing Constrained by Seaward Shallow-Water Sediment Drift Architecture (ODP Leg 194, Marion Plateau)

by

Stephen P. Obrochta

A thesis submitted in partial fulfillment
of the requirements for the degree of
Master of Science
College of Marine Science
University of South Florida

Major Professor: Albert C. Hine, Ph.D.
Benjamin P. Flower, Ph.D.
Pamela Muller, Ph.D.
Gregg R. Brooks, Ph.D.

Date of Approval:
July 9, 2004

Keywords: australia, great barrier reef, isotope, leg 194, ocean drilling program, odp, site 1198

Acknowledgements

Completion of this thesis would not have been possible without the love and support of my wife, Mariko Sakamoto.

My thesis committee, Drs. Albert C. Hine, Benjamin P. Flower, Pamela Muller, and Gregg R. Brooks, each experts in their respective fields, provided essential guidance and advice, for which I am grateful. My advisor, Dr. Hine, tirelessly sought, from many different sources, the means for completing this thesis. Dr Hine also provided a superb research facility, stocked with state-of-the-art equipment, as well as the financial support necessary to effectively utilize such a facility. In addition, Dr. Hine, provided many foreign and domestic travel opportunities, broadening my scientific and cultural knowledge. Dr. Stan Locker, although not an official member of my committee, contributed significant time, resources, and knowledge to my thesis and cheerfully created time to advise on numerous occasions.

I am very thankful to the many people who helped tremendously with this project. This includes Beau Suthard and Bret Jarrett who spent many hours discussing this thesis with me. Discussion with Jennifer Smith and other members of the paleoceanography and paleoclimatology group helped solidify the major themes of this work. Dr. Michael W. Howell provided the X-Ray diffractometer, a fundamental tool of this study, and Dr Robert Halley advised on the interpretation of it's results. Dr. Terry Quinn and Ethan Goddard were essential to the completion of the geochemical analyses. Drs. David Hollander and Robert Byrne also deserve thanks for providing the coulometer used in this study. Finally, I express my thanks to all others who contributed in tangible and intangible ways to the completion of this manuscript.

This research was funded by Ocean Drilling Program Leg 194 post-cruise funds provided to Dr. Hine.

Table of Contents

List of Tables

List of Figures

Australian Great Barrier Reef Initiation Timing Constrained by Seaward Shallow-Water Sediment Drift Architecture (ODP Leg 194, Marion Plateau)

Stephen P. Obrochta

## ABSTRACT

I resolved the sedimentary architecture of a shallow water (< 500 m), hemipelagic sediment drift located on the Marion Plateau, seaward and downstream of the Great Barrier Reef (GBR). The drift responded increasingly to sea-level fluctuations during the Pleistocene. In the early Pleistocene, local climatic variations introduce a precessional rhythm to drift architecture that is out of phase with sea level-forced cyclicity. Beginning in the mid Pleistocene, sea level variations dominate drift architecture, with the highest carbonate and terrigenous fluxes likely occurring during highstand and transgression, respectively. At the sea-level transgression of MIS 15 and subsequent isotope stages, the phasing of maximum terrigenous flux corresponds to sea-level transgression, indicating siliciclastic sediment accumulated on the continental shelf behind an exposed barrier reef during the lowstand of MIS 16 and was remobilized by rising sea-level. These sedimentological data indicate GBR initiation occurred during MIS 17. The normal polarity exhibited by the central GBR and thick section of underlying sediments rules out initiation during MIS 19.

MIS 17 was the first of the asymmetric glacial cycles characteristic of the Late Pleistocene. If the Florida Keys and Belize barrier reef initiations were indeed simultaneous with that of the GBR, then the changing nature of cyclicity in global sea level and climatic fluctuations likely influenced the initiation of the world's major, modern barrier reefs.

# INTRODUCTION

Initiation of many of the world's major modern barrier reefs occurred during the Brunhes Chron (past 780 k.y.), including the Belize barrier reef, the Florida Keys barrier reef, and the Australian Great Barrier Reef (GBR) (Fig. 1) (Droxler and Farrell, 2000; International Consortium, 2001; Droxler et al., 2002; Multer et al., 2002; Droxler et al., 2003b). Given the resolution of the applicable dating techniques, these reefs were perhaps synchronously initiated. A higher-resolution chronology is needed for each reef to constrain the timing of reef initiation.

In this study, I resolved the mixed carbonate-siliciclastic sedimentary architecture of a shallow (< 500 m) continental margin sediment drift located seaward and downstream of the GBR. The sediment drift is ideally positioned to record the timing of reef initiation as the nature of off-shelf sedimentation changed in response to the evolution of a rimmed margin and 100-k.y. ice sheets. Over the course of a sea-level cycle, the timing of the maximum off-shelf flux of sediment is different but predictable on rimmed (e.g., Dunbar et al., 2000) and non-rimmed shelves (Wilson, 1967). The point at which the timing of sediment flux off the northeast (NE) Australia continental shelf corresponded to that of a rimmed margin likely indicates GBR initiation. Whether this timing is coincident with global events, as proposed by the International Consortium for Great Barrier Reef Drilling (2001), or changing regional environmental parameters (e.g., Isern et al., 1996), will provide additional clues to the mechanisms responsible for the initiation of the GBR specifically and to that of late Quaternary reefs in general.

## Platform Morphological Controls on Off-Shelf Sedimentation

The NE Australia shelf is an emergent, rimmed bypass-margin (Read, 1982; James and Mountjoy, 1983; Tucker and Wright, 1990). In such a setting, high sea level

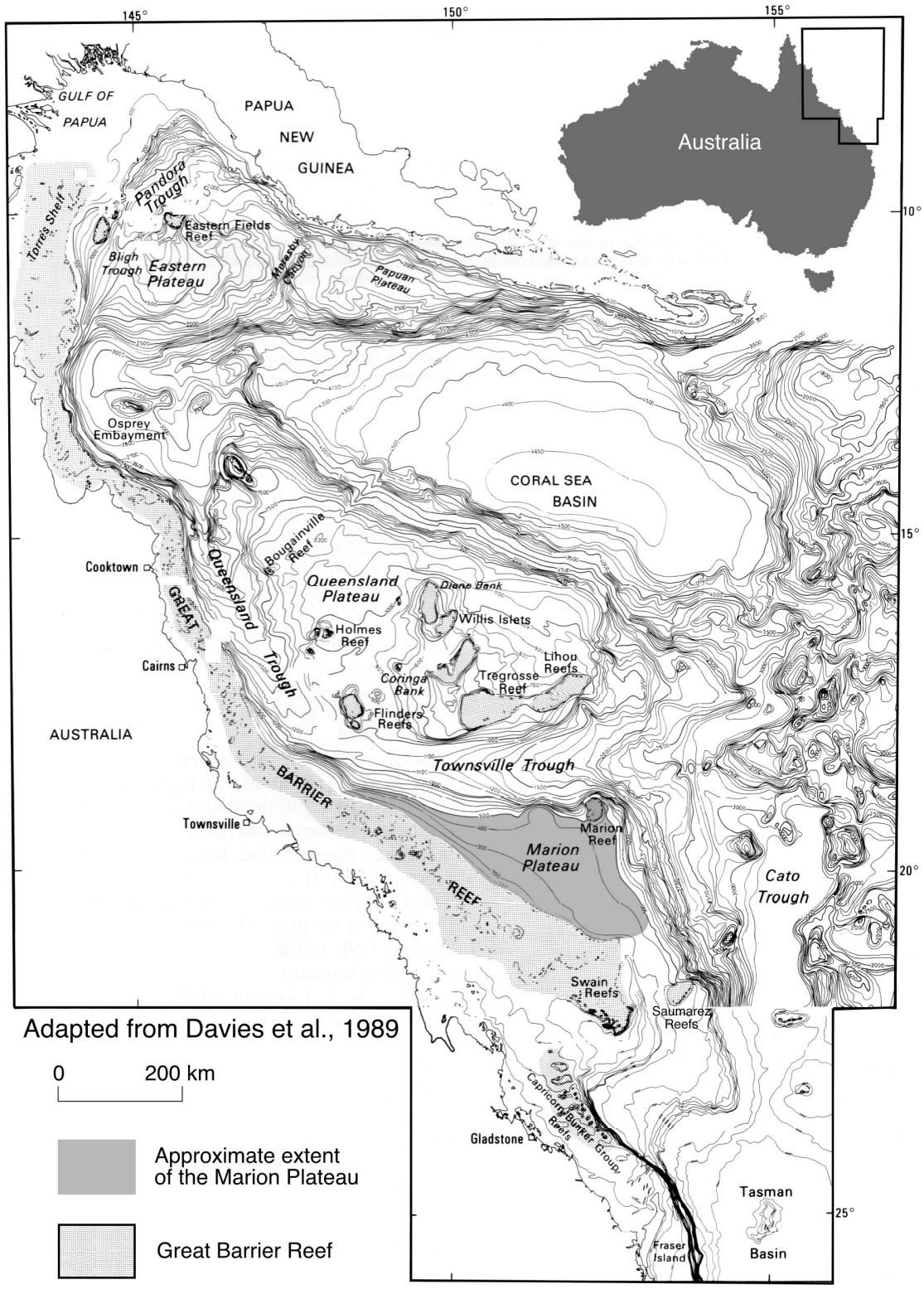


Fig. 1. Overview map of the Coral Sea basin showing the Great Barrier Reef and the Marion Plateau. Adapted (Davies et al., 1989).

floods the top of the platform, maximizing sediment production (e.g., Hine et al., 1981; Boardman and Neumann, 1984; Droxler and Schlager, 1985; Boardman and Neumann, 1986), while shed carbonate sediments bypass the steep slope and are directly deposited in deep basins. During sea-level lowstand, the shelf-break and barrier reef are exposed, effectively shutting down carbonate sediment production.

Prior to the Brunhes Chron, the NE Australia margin probably lacked a rim, perhaps exhibiting a morphology closer to that of a ramped margin. Below the GBR are prograding fluviodeltaic deposits (Symonds et al., 1983). Such a ramp to rim transition may be reflected in the nature of off-shelf sedimentation. For example, a fundamental change in the nature of cyclic lithological variations within sediment drifts along the leeward side of the Great Bahama Bank (GBB) occurred in the Pliocene (Beach and Ginsburg, 1980; Eberli, Swart, Malone, et al., 1997) due to a change in platform morphology (Isern and Anselmetti, 2001). The Miocene carbonate ramp facies of the GBB display a symmetric lithologic response to sea level as the locus of maximum sediment production shifted laterally up and down the slope. After the Pliocene development of a rimmed platform morphology, cyclic lithological variability within the sediment drift became asymmetric (saw-toothed) in shape. Once rising sea level flooded the platform top, neritic sediment production and shedding rapidly increased. As sea level fell, erosion of platform-top neritic material produced a more gradual lithological change.

In NE Australia, rivers fueled by the Queensland rainforests discharge significant amounts of quartz and clay to the continental margin, creating the world's largest extant mixed carbonate-siliciclastic depositional system (Maxwell and Swinchatt, 1970; Davies et al., 1989). Off-shelf sedimentation in such a setting is often described by the concept of reciprocal sedimentation (Wilson, 1967). Such a model treats the carbonate and siliciclastic components separately as pure end-members, with the shelf behaving like a carbonate platform during sea-level highstand and like a siliciclastic shelf during sea-level lowstand when rivers incise the shelf discharging their sediment load directly to the slope (e.g., Vail et al., 1977; Posamentier and Vail, 1988; Van Wagoner et al., 1988; Posamentier et al., 1992).

Recent work has shown that the presence of a barrier reef also exerts a major control on terrigenous off-shelf sedimentation. Rather than incising the shelf during lowstand, the late Quaternary rivers of NE Australia are thought to aggrade due to the presence of an exposed barrier reef, storing their sediment load on the shelf (Woolfe et al., 1998). The carbonate buildups create a barrier to flow and decrease the gradient that would otherwise be enhanced during lowstand. Thus, a simple reciprocal sedimentation model does not apply to NE Australia since GBR inception (Dunbar et al., 2000; Dunbar and Dickens, 2003a; b; Page et al., 2003; Page, *in press*). In these studies, carbonate-poor intervals identified in sediment cores from slopes and basins seaward of the GBR did not correlate to high terrigenous sediment accumulation during sea-level lowstand. Rather, the highest accumulation of terrigenous material occurs during sea-level transgression when siliciclastic material trapped behind an exposed barrier reef is remobilized as the continental shelf is flooded by rising sea level (Fig. 2). This relationship has been observed, with independent sea level control provided by oxygen isotopes, to the termination of Marine Isotope Stage 8 (MIS 8) and subsequent sea-level transgression beginning MIS 7 (Dunbar et al., 2000).

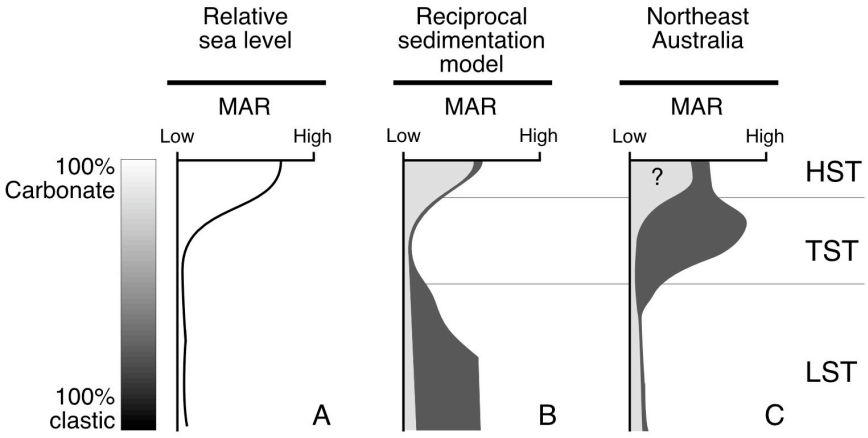


Fig. 2. Off-shelf transport of sediment in mixed carbonate/siliciclastic systems. A) Relative sea level. B) Traditional reciprocal sedimentation. C) Northeast Australia coast, as a function of a rimmed platform. MAR refers to mass accumulation rate. Adapted from Page et al. (2003).

Coring results from Ribbon Reef 5 in the central GBR indicate that a rimmed platform morphology did not exist prior to the Brunhes-Matuyama boundary (780 ka) (International Consortium, 2001). The core exhibits an entirely normal magnetic polarity, and strontium isotope data from the base indicate an age of 600 ± 280 ka. However, the nature of off-shelf sedimentation prior to GBR initiation has yet to be examined.

## Late Cenozoic Sea-Level Fluctuations

Passive margin sedimentary sequences are created primarily by relative sea level changes produced by the interaction of local tectonics with global eustatic sea level (e.g., Vail et al., 1977), which in turn, has been controlled since the late Neogene by the waxing and waning of northern hemisphere ice sheets. During the late Pliocene and early Pleistocene, the dominant period of these glacial/interglacial cycles was 41 k.y. These glacial cycles were symmetric (equivalent times required for glaciation and deglaciation) and appeared to be a linear response to obliquity forcing, although it has been recently noted that precession, which dominates insolation at any latitude, is conspicuously absent from the $\delta^{18}O$ records of the 41-k.y. world (Raymo and Nisancioglu, 2003).

A gradual transition to a 100-k.y. period, which is the same as that of orbital eccentricity, occurred during the mid Pleistocene. This change, often referred to as the Mid Pleistocene Climate Transition (MPCT), consisted of two events. 1) a 40-k.y. duration increase in $\delta^{18}O$ centered at ~ 922 ka (MIS 22) was followed by 2) the onset of 100-k.y. cycles at ~ 641 ka (MIS 16) (Mudelsee and Schulz, 1997). By MIS 17, glacial/interglacial cycles began to exhibit a saw-tooth character (e.g., Shackleton and Hall, 1989), with a slow deterioration into glacial conditions followed by rapid warming. Significant precessional frequencies are present in the glacial/interglacial-scale $\delta^{18}O$ excursions of the 100-k.y. world. These excursions also exhibit an increased amplitude, which is commonly attributed to larger ice volume post-MPCT (Berger and Jansen, 1994). Because eccentricity forcing is weak, the exact mechanism and system of feedbacks responsible for the 100-k.y. glacial cycles is unknown (Imbrie et al., 1993).

## Sediment Drifts

Sediment drifts, often referred to as contourites, typically form along western basin boundaries in the deep sea where bottom currents smooth and rework sediment gravity flows in contour-parallel features (Hollister et al., 1978). For a drift to form, an ample sediment supply must exist along with a current swift enough to entrain this sediment and later deposit it as the current looses competency. Drift deposition typically occurs in areas were sea floor topography causes the current to decelerate. However, the very reason for a drift's existence complicates it's interpretation, as fluctuating current speed may rework and slump sediment. Variations in current speed along with the type and supply of sediments available to the drift often produce a regular or cyclic sedimentary architecture. The architecture of a sediment drift describes how the varying components are assembled into layers and how those layers relate temporally and spatially.

In general, sediment drifts do not accumulate on upper continental margins due to the lack of accommodation space and currents that typically scour. In addition, large-amplitude sea-level regressions of the late Pleistocene have eroded much of the previously deposited sediment from continental shelves, leaving most modern shelves with only a thin veneer of Holocene sediment. Several modern sediment drift systems exist on upper continental margins, however. In the northern Straits of Florida, Mullins et al. (1980) identified drifts on the leeward side of the Bahamas Banks. Antarctic continental shelf drifts have been interpreted to form as a result of local eddies or gyres (i.e., current deceleration) (Harris et al., 1999; Harris et al., 2001). A massive contourite system in the Gulf of Cadiz, west of Gibraltar has formed as Mediterranean Outflow Water deposits entrained sediment (e.g., Hernandez-Molina et al., 2003)

# Study Area

## Marion Plateau

The 77,000-km$^2$ Marion Plateau (MP) is located directly seaward of the south-central GBR, between 18˚ S and 23˚ S latitude, and was drilled on Ocean Drilling Program (ODP) Leg 194 (Fig. 3). The MP is located seaward of the south-central GBR, between 18˚S and 23˚S latitude with an area of ~ 77,000 km$^2$ (Davies et al., 1989). This structurally-controlled terrace is bounded by the GBR to the southeast, the Queensland Trough to the north, and the Cato Trough to the east, and is slowly subsiding linearly along with the rest of the NE Australia margin in the Quaternary (Isern, Anselmetti, and Blum et al., 2002). The MP extends the continental shelf into the Coral Sea, yet remains between 300 and 500 meters below sea level (mbsl), which is above the carbonate compensation depth and the zone of the continental slope commonly disturbed by gravity flows. The MP was an exposed continental block until the latest Paleogene, when it was flooded by rising sea-level (Pigram et al., 1992). ODP Leg 194 Sites 1194, 1193, 1197, and 1198 penetrated this basement, recovering volcaniclastic material (Isern, Anselmetti, Blum et al., 2002). Reef growth was initiated in the early Miocene, with abundant flourishing reefs by the mid Miocene (Davies, McKenzie, Palmer-Julson et al., 1991). These reefs drowned by the late Miocene (Isern, Anselmetti, Blum et al., 2002). From the latest Miocene, hemipelagic sediment deposited under the influence of the East Australian Current (EAC) has completely infilled the existing topographic depressions between drowned carbonate platforms of the MP (Fig. 4). The resulting stratigraphic succession of horizontally-overlapping, vertically-stacked sediment drifts reaches a maximum thickness of 200 m thick at Site 1198 with sedimentation rates on the order of 10 cm/k.y. (Shipboard Scientific Party, 2002).

Adjacent to the study area, the EAC is weak and poorly organized relative to other western boundary currents, such as the Gulf Stream (Andrews and Furnas, 1986). Of the 24 Sv (1 Sv = $10^6$ m$^3$/s) of baroclinic influx within the upper 1000 m provided by

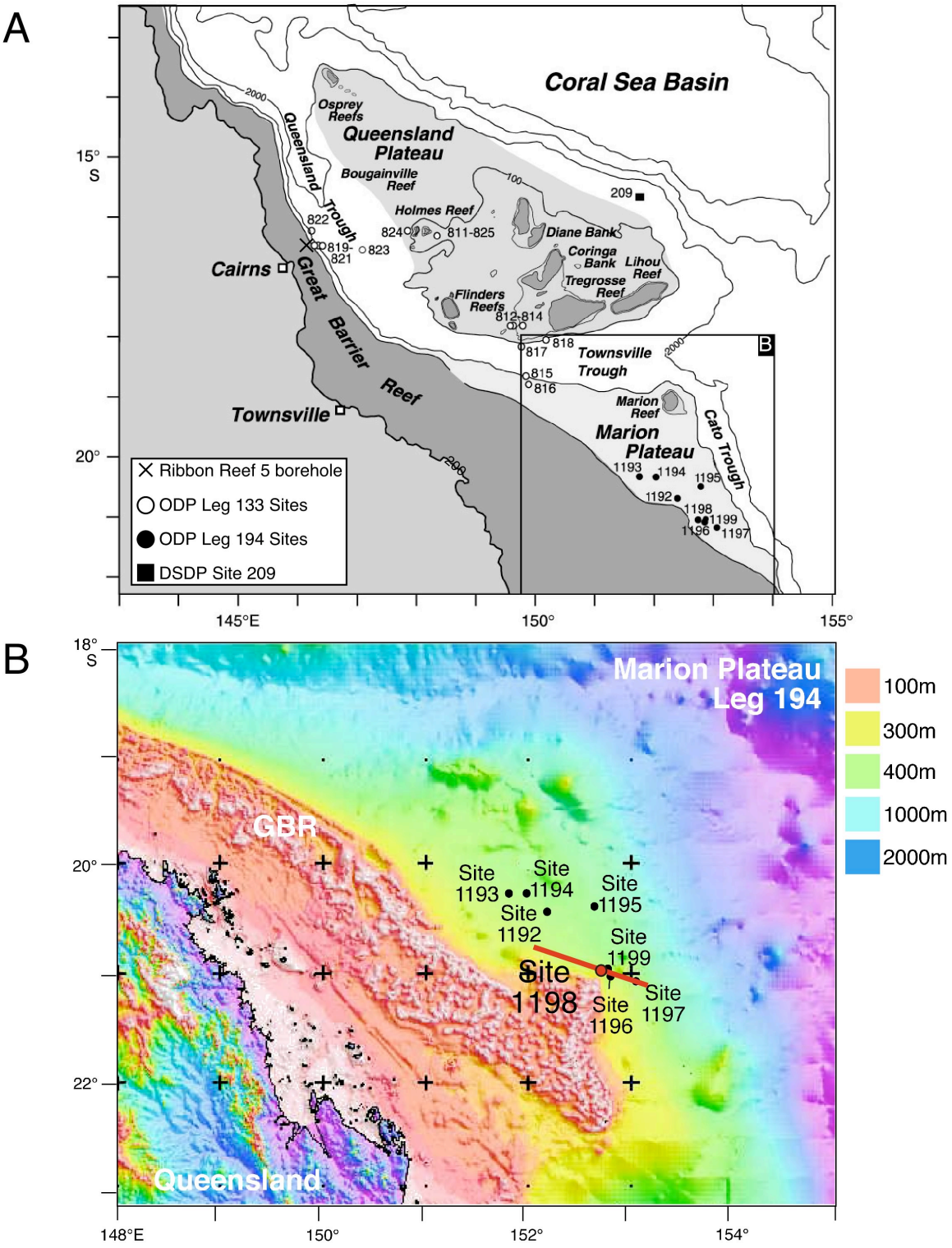


Fig. 3. A) South-central Great Barrier Reef showing location of ODP and DSDP cores, as well as the Ribbon Reef 5 borehole. Adapted from (Isern, Anselmetti, Blum, et al., 2002) B) Bathymetry map of the Marion Plateau. Depths are approximate. Adapted from (Shipboard Scientific Party, 2002)

the South Equatorial Current to the Coral Sea, only 6 Sv of water directly feeds the EAC (Andrews and Clegg, 1989). Geostrophic profiles across the EAC adjacent to the Marion Plateau indicate current speeds of 10 cm/s (Andrews and Clegg, 1989) to 70 cm/s (Church, 1987). However, the main flow of the EAC is typically deflected east by the Marion Plateau, driving a weak cyclonic (clockwise) eddy above the platform (Church, 1987; Griffin et al., 1987; Andrews and Clegg, 1989; Middleton et al., 1994; Burrage et al., 1996).

Site 1198

This study was conducted on the upper 100 m of sediment from Site 1198 (20.967˚ S, 152.733˚ E; 319 mbsl; Figs. 3, 4) which penetrated the thickest portion of the Pliocene to Pleistocene hemipelagic sediment drift (Fig. 4b). The drift section at Site 1198 extends to 200.6 mbsf, comprising an entire seismic megasequence (MS) (MS D of Isern, Anselmetti, Blum et al., 2002) and one lithostratigraphic unit (Unit 1 of Shipboard Scientific Party, 2002). This unit consists of a succession of light gray to olive-gray, moderately well-sorted wackestones, packstones, and grainstones, and is divided into two subunits on the basis of sedimentary texture, lithology, and structure, as well as biotic assemblage (Shipboard Scientific Party, 2002). Subunit 1A extends from 0 to 62.0 mbsf and alternates between a dark greenish gray skeletal wackestone and a light gray grainstone texture with evidence of minor synsedimentary slumping. Pelagic sediments, mainly comprised of foraminifers with a smaller amount of pteropods, dominate the skeletal component of this subunit. Minor amounts of benthic foraminifers, echinoderm fragments, and scaphopods are present. The transition to Subunit 1B, which extends to the base of MS D at 200.6 mbsf, is marked by a thin layer of light greenish mud. This subunit exhibits a packstone texture dominated by planktonic foraminifers.

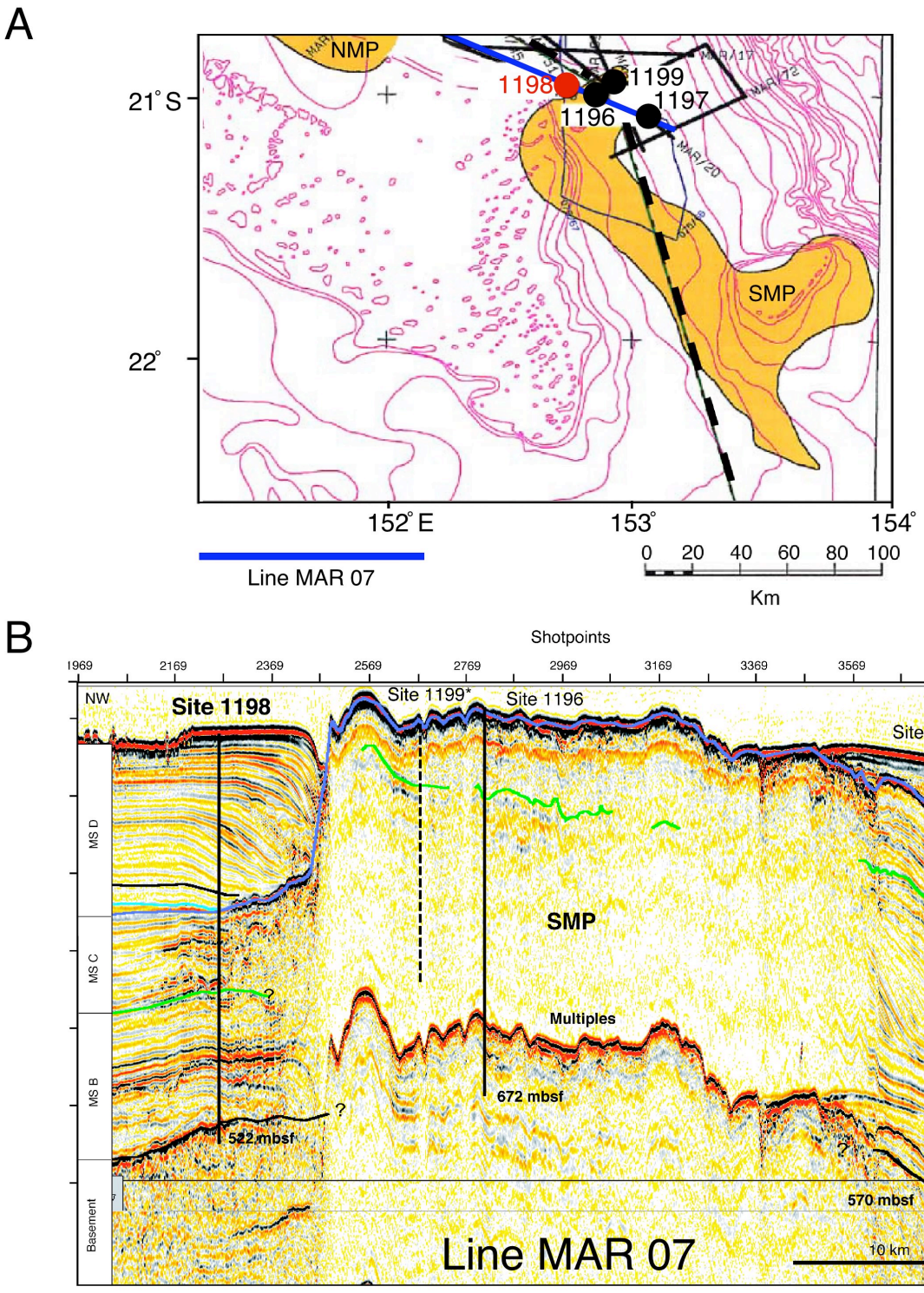


Fig. 4. A) Close-up of the Marion Plateau showing the extent of the Southern Marion Platform (SMP), a portion of the Northern Marion Platform (NMP), and ODP Leg 194 Sites. Site 1198, shown in red, was used for this study. Seismic line MAR 07 is shown in blue. B) Seismic line MAR 07 showing position of Sites around the SMP. Megasequence D (MS D) refers to the hemipelagic sediment drift analyzed for thisstudy. Adapted from (Isern, Anselmetti, Blum, et al., 2002).

## HYPOTHESIS AND SCIENTIFIC OBJECTIVES

I propose that the Marion Plateau hemipelagic (< 500 m) sediment drift located seaward and downstream of the Great Barrier Reef (GBR) exhibits a cyclic, predictable sedimentary architecture that changed in response to the development of a rimmed margin morphology and to the evolution in the period of eustatic sea-level fluctuations from 41 k.y. to 100 k.y. The timing of the architectural changes, as determined by oxygen isotope stratigraphy, likely corresponds to GBR initiation. Specific objectives include:

- Generating a planktonic foraminiferal $\delta^{18}O$ time series to provide age and sea-level control.
- Calculating mass accumulation rates (MARs) of the primary drift constituents to determine the absolute flux of each constituent.
- Resolve the sedimentary architecture of the drift during the early and late Pleistocene by examining MAR and $\delta^{18}O$ data to determine the timing of maximum sediment accumulation relative both to phases of a sea-level cycle and to absolute age

# METHODS

This study is conducted on sediment samples from ODP Leg 194 Hole 1198A. An identical suite of quantitative analyses was performed on two lithological sections, an early Pleistocene, Matuyama (41-k.y. world) section (62.15 – 100.1 mbsf; ~ 1.1 – 1.7 Ma) from within Subunit 1B (Shipboard Scientific Party, 2002) and a mid to late Pleistocene, Brunhes (00-k.y. world section) (14.5 – 41.11 mbsf; ~ 340 – 770 ka) from within Subunit 1A (Shipboard Scientific Party, 2002) (Table 1).

| Interval | Depth (mbsf) | | Age (ka) | | Core | |
|---|---|---|---|---|---|---|
| | Top | Bottom | Top | Bottom | Top | Bottom |
| Page (*in press*) | 0.04 | 14.5 | ? | 340 | 1H | 3H |
| Brunhes | 14.5 | 41.11 | 340 | 770 | 3H | 5H6W15 cm |
| Matuyama | 62.15 | 100.1 | 1100 | 1700 | 8H | 11H |

Table 1. Intervals of the sediment drift at ODP Hole 1198A that were analyzed for this study. The interval analyzed for %$CaCO_3$ by Page (*in press*) is included. Abbreviations used include H (advanced hydraulic piston core) and W (working half). Each core and section are 9.5 m and 150 cm in length, respectively.

## Oxygen Isotopes

Stable oxygen isotopic ratios ($\delta^{18}O$) were determined on ~ 4 (35 – 80 $\mu$g) tests (355 to 250 $\mu$m) of the planktonic foraminifer *Globigerinoides ruber* (white variety) with a dual inlet stable isotope Delta Plus XL mass spectrometer at the University of South Florida, College of Marine Science Mass Spectrometry Laboratory. The tests were briefly (~ 10 s) ultrasonically cleaned in methanol, allowed to dry, and weighed prior to analysis. Sampling interval ranged between 15 and 30 cm (average 22 cm) for Subunit 1B and was 25 cm for Subunit 1A.

## Stratigraphy and Chronology

The sediment drift was not advanced piston cored at Hole 1198B, preventing the construction of a composite depth scale. As a result, sediment was likely lost between each 9.5 m-long core. However, sediment expansion after recovery commonly resulted in overlap between cores. This problem was most apparent in the shipboard color reflectance dataset (Fig. 5). The depth of the strigraphically lower core was shifted down, creating an apparent continuous record in the depth domain. The resulting depth scale is referred to as adjusted meters below sea floor (ambsf) (Table 2).

| Core | Adjustment |
|---|---|
| 1H | 0 m |
| 2H | 0 m |
| 3H | 0 m |
| 4H | 0 m |
| 5H | + 0.20 m |
| 6H | + 0.35 m |
| 7H | +0.35 m |
| 8H | + 0.55 m |
| 9H | + 0.55 m |
| 10H | + 0.75 m |
| 11H | + 0.75 m |

Table 2. Adjustments made to the meters below seafloor (mbsf) depth scale of Unit 1 at Hole 1198A to produce the adjusted mbsf (ambsf) scale.

The shipboard age model was refined by correlating the planktonic foraminifer oxygen isotope record of this study (Fig. 6) to the astronomically tuned benthic foraminifer oxygen isotope time series of ODP Site 677 (Shackleton et al., 1990) (available online at http://delphi.esc.cam.ac.uk/) (Fig. 7). This was accomplished with the Macintosh program AnalySeries 1.2 (Paillard et al., 1996) and resulted in the conversion of the 1198A record from the depth domain to the time domain. The overall shape and amplitude in the Hole1198A marine isotope stages fits well that of Site 677. The large amplitude (> 0.5‰) $\delta^{18}O$ variations in both records are interpreted to primarily reflect glacial/interglacial-scale changes in ice volume changes (i.e. eustatic sea level).

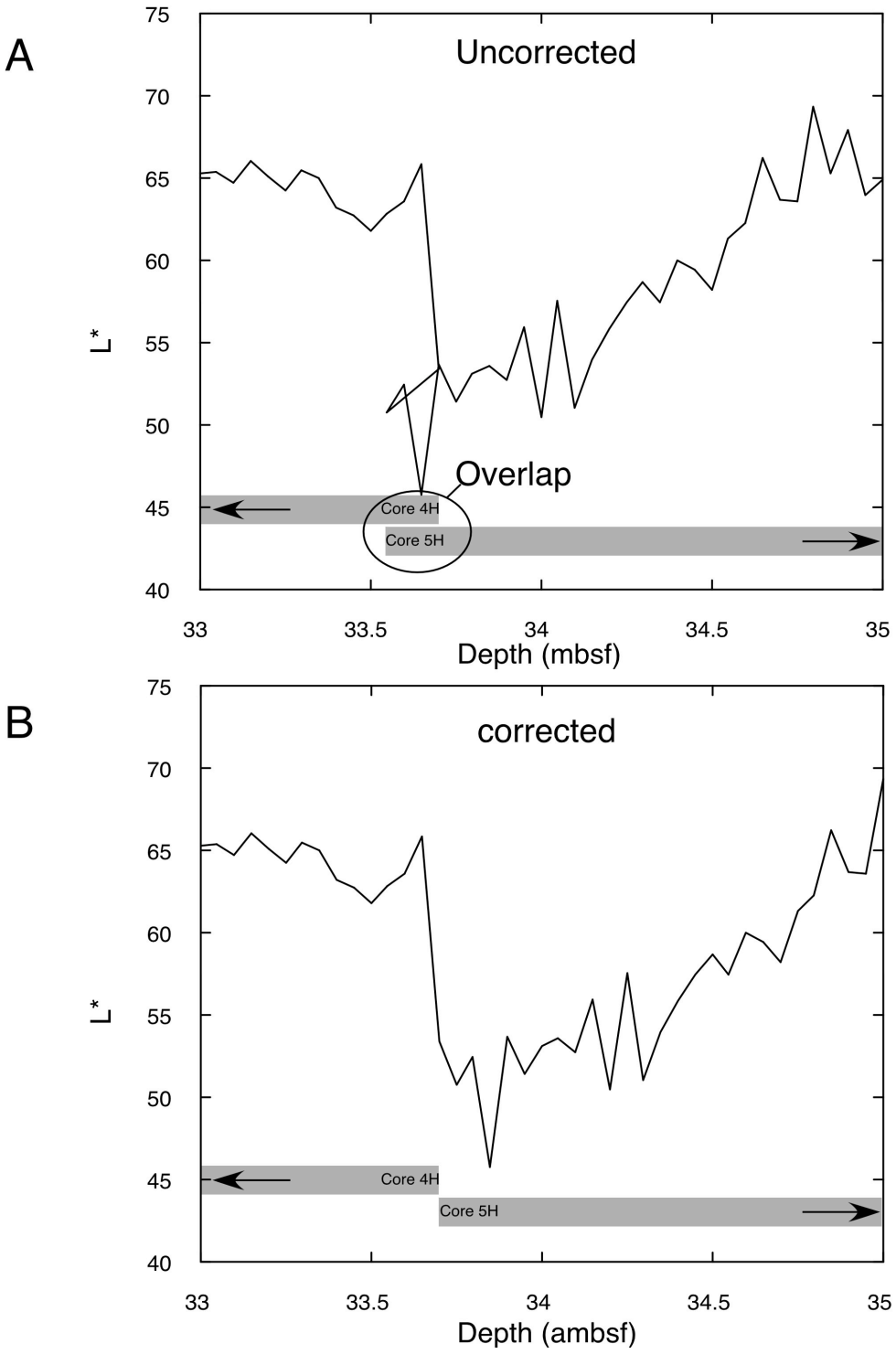


Fig. 5. A) Example of core overlap in Hole 1198A in the mbsf depth scale. This is likely a product of core expansion after recovery. B) Example of Hole 1198A in the ambsf (adjusted meters below seafloor) depth scale, which corrects for the apparent overlap by shifting moving the stratigraphically lower core below the bottom of the upper core.

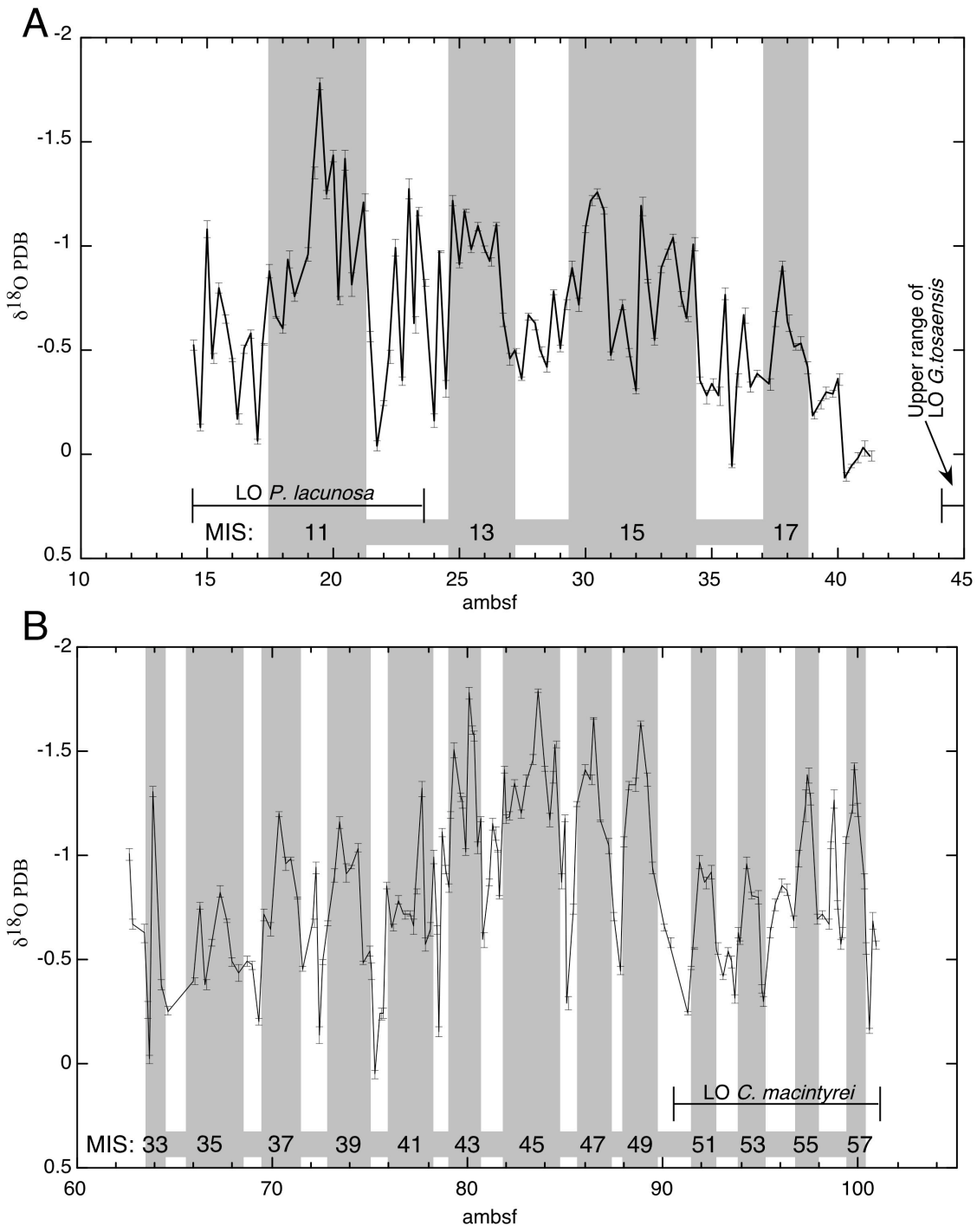


Fig. 6. *Globigerinoides ruber* $\delta^{18}O$ record in adjusted meters below seafloor (ambsf) domain of the two intervals of Hole 1198A with marine isotope interglacial stages shaded. Error bars on $\delta^{18}O$ record indicate analytical standard deviations. Biostratigraphic datum levels are also indicated.

Marine Isotope Stages 10 – 17 and MIS 31 – 58 were resolved. The $\delta^{18}O$ age model is consistent with the shipboard age model.

The shipboard age model for Site 1198A was based solely on biostratigraphic data (Table 3), primarily from core-catcher samples (Shipboard Scientific Party, 2002). Paleomagnetic data were not included due to difficulties analyzing whole-round core sections in the 1 – 2 m heave conditions experienced at Site 1198 (Shipboard Scientific Party, 2002). The paleomagnetic data are mostly uninterpretable. Regardless of the problematic paleomagnetic data the shipboard scientists placed the Brunhes-Matuyama boundary (780 ka) at ~ 52 ambsf. In the oxygen-isotope refined age model, 780 ka occurs at ~ 42 ambsf (Fig 8).

| Datum Level | Core, Section, Interval (Upper / Lower) | Depth of first absence or presence (ambsf) | Depth of last presence of absense (ambsf) | Age (Ma) |
|---|---|---|---|---|
| ACME *Emiliania. huxleyi* | Core top / 1H2W-80 cm | 0.00 | 2.3 | 0.08 |
| LO pink *Globigerinoides. ruber* | 1H4W-20 – 22 cm / 1H-CC | 4.70 | 4.95 | 0.120 |
| FO *Emiliania. huxleyi* | 1H-CC / 2H2W-80 cm | 4.87 | 7.3 | 0.26 |
| LO *Puedoemiliania. lacunosa* | 2H-CC / 3H-CC | 14.52 | 23.78 | 0.46 |
| LO *Globorotalia. tosaensis* | 5H-CC / 6H-CC | 44.08 | 52.59 | 0.65 – 0.8 |
| LO *Calcidicsus. macintyrei* | 10H-CC / 1H-CC | 90.61 | 101.01 | 1.59 |

Table 3. Shipboard biostratigraphic datum levels used to create shipboard age model. LO and FO refer to last observance and first observance, respectively. CC refers to core catcher. Depth is in adjusted mbsf domain (ambsf).

## X-Ray Diffraction

X-Ray diffraction (XRD) analysis was performed with a Bruker AXS D4 Endeavor, which is equipped with a sample changer capable of automating the analysis of 60 samples. Quantitative percentages of aragonite (ARA), low-Mg calcite (LMC), and high-Mg calcite (HMC) were determined by the same method used for ODP Leg 182 (Great Australian Bight) (Feary, D. A., Hine, A. C., Malone, M. J., et al., 2000).

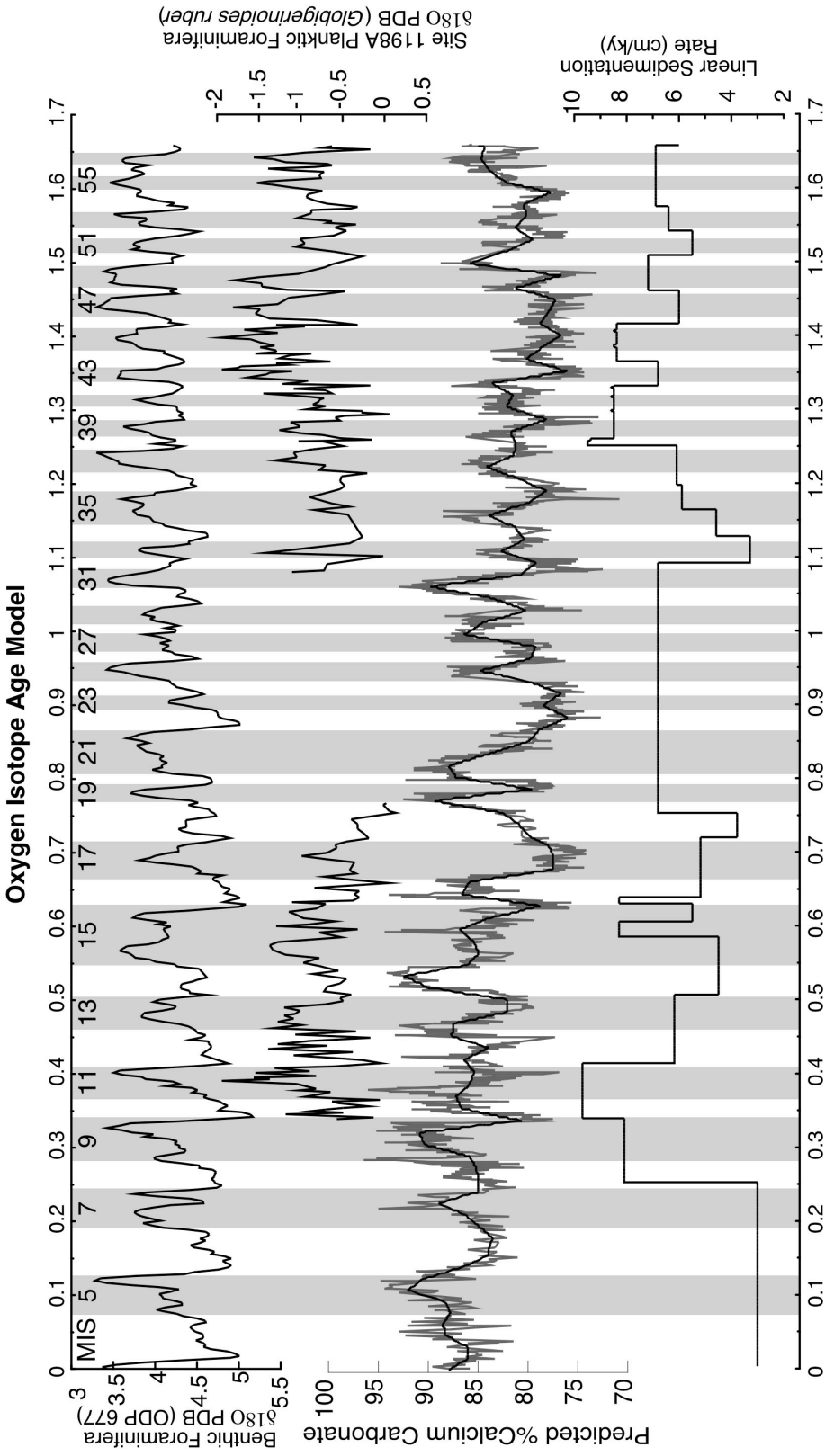


Fig. 7. A) Age model of Hole 1198A correlated to ODP Site 677 and resulting linear sedimentation rates as determined by AnalySeries (Paillard et al., 1996). Shaded areas represent interglacial intervals and are based on Site 677. Glacial/interglacial-scale vairions in $\%CaCO_3$ predicted from color reflectance data correspond well to )DP 677 Marine Isotope Stages .

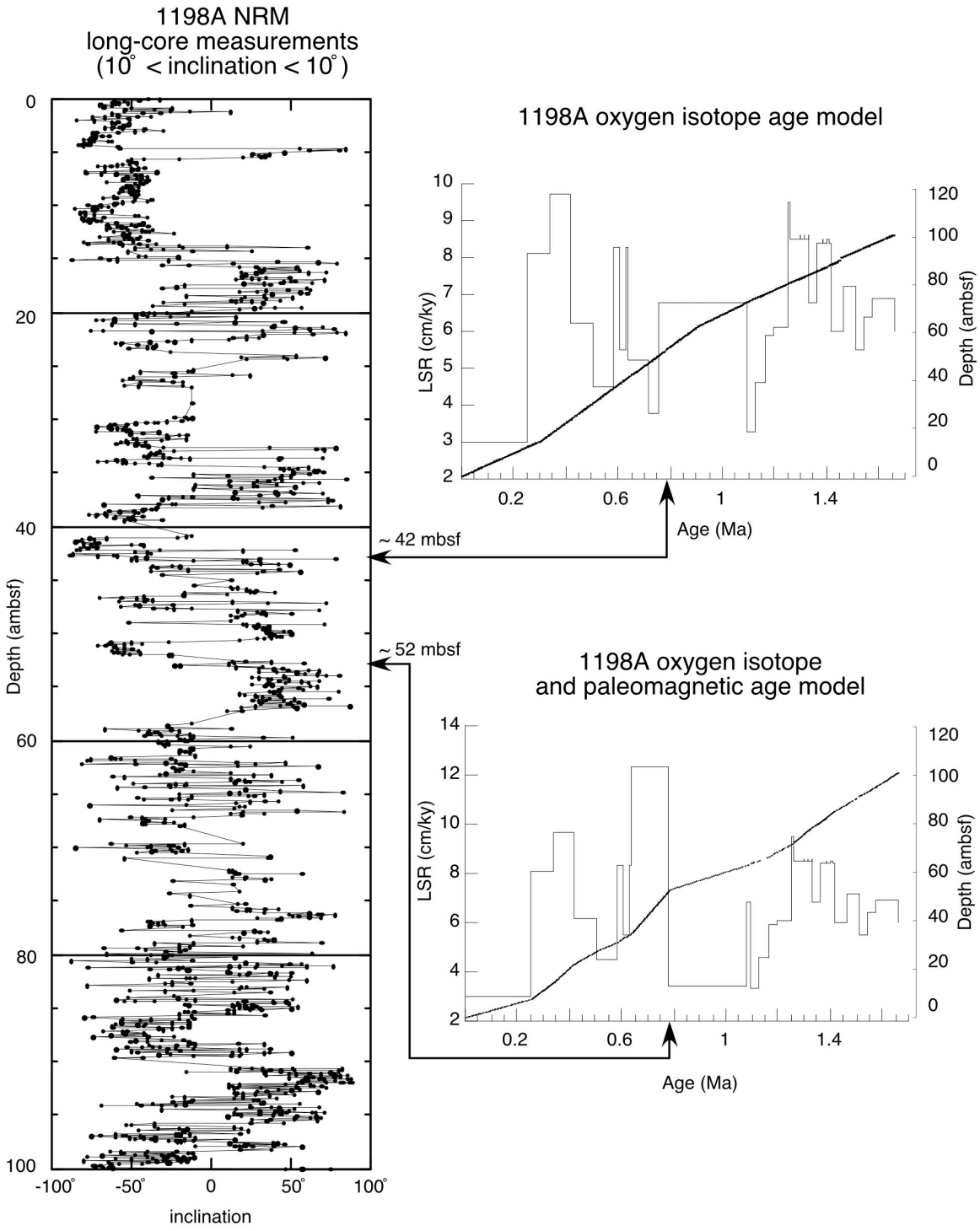


Fig. 8. Long-core paleomagnetic data, excluding measurement ± 10°, from Hole 1198A. 780 ka falls 10 ambsf above the shipboard placement of the Brunhes-Matuyama boundary. Placing the 780 ka at 52 ambsf results in large fluctuations in LSR.

This method has an error of ± 5% (Swart et al., 2002). Sampling interval was 15 cm and 25 cm for Subunits 1B and 1A, respectively. Approximately 3 to 4 g of bulk sample was crushed and homogenized with a mortar and pestle, packed into powder mounts, and scanned from 24 to 32.2°2θ at a 0.02° step for 2 seconds per step while spinning the sample at 60 rpm. Spinning the sample reduces the effect of preferential orientation. The Cu Kα X-Ray generator was run at 40 kV and 40 mA. That a sample is comprised of only the above-mentioned minerals (i.e., ARA + LMC + HMC = 1) is assumed. Standards were prepared by mixing known amounts of the pure form of these minerals. These standards were analyzed under the same conditions as the samples, and the slope of the relationship between the intensity ratios (i.e., peak areas) and concentration ratios of the standards was determined. Once this slope was quantified, it is used in an equation together with the intensity ratios of the samples to solve for mineral percentages within the calcium carbonate fraction.

Smear slides of the clay (< 2 $\mu$m) fractions of selected samples were scanned from 24 - 32.2°2θ and 2 - 40°2θ, respectively. The other scan parameters were identical as the bulk powder scans. Silt was separated from clay by centrifuge (1000 rpm for 2.5 minutes). The supernatant clay-sized particles were decanted and centrifuged at 16,000 rpm for 14 minutes to settle particles > 0.05 $\mu$m in size. Calcium carbonate was present in the < 2 $\mu$m size fraction, but the slides were made of only the finer-sized, dark-colored, non-carbonate fraction. Selected clay samples were rescanned after exposure to ethylene gylocol for > 24 hours.

Percent Calcium Carbonate (Coulometry)

The percentage of $CaCO_3$ was determined on a split of the same bulk, powdered sample used for XRD analysis. A measured amount of sample (typically ~ 15 mg) was acidified by weak percholric acid, and the resulting $CO_2$ gas was analyzed to determine the amount of inorganic carbon. Stochiometic relationships are used to determine the amount of $CaCO_3$. X-Ray diffraction results indicate that no other carbonate minerals, such as carbonate flourapatite are significantly present.

A UIC CM5014 Coulometer equipped with a CM5130 acidification module was used to determine percent calcium carbonate. A split of the crushed bulk powder prepared for XRD analysis was dehydrated in a drying oven for 24 hours, and sampling intervals are the same as for XRD analysis. After being removed and allowed to equilibrate for 1 hour, the sample was homogenized, and approximately 15 mg was removed, weighed with an analytical balance, and placed into a sample vial for analysis. Weak perchloric acid was used to dissolve the $CaCO_3$ within a sample. The evolved $CO_2$ gas was captured and analyzed by the coulometer, which reports inorganic carbon mass ($\mu$g).

For each day of analyses, the coulometer was calibrated with at least 4 pure $CaCO_3$ standards. The mass of inorganic carbon within each standard was determined based on stoichiometery (i.e., 12%), which was regressed against the coulometer output (carbon mass in $\mu$g). The resulting equation was used to determine percent inorganic carbon (%IC) based on the relationship $\%CaCO_3 = \%IC * 8.333$ (Mix et al., 1995). A new equation was determined for each day of usage. Standards were run every 10 samples, and a duplicate sample was run every 20 samples and/or at the end of the day's run. Sampling interval was 15 cm and 25 cm for Subunits 1B and 1A, respectively.

## Predicted Percent Calcium Carbonate (Color Reflectance)

Multiple linear regressions of the raw shipboard color reflectance data (5 cm sampling interval) and $\%CaCO_3$ data (15 – 25 cm sampling interval) were used to predict $\%CaCO_3$ in the unanalyzed section (41.35 – 62.7 ambsf). The $\%CaCO_3$ data include 1) the series of Page (*in press*) from 0.04 to 14.5 ambsf, 2) the 100-k.y. world series from 14.5 to 41.35 ambsf, and 3) the 41-k.y. world series from 62.7 to 100.85 ambsf. Page (*in press*) used a carbonate bomb to determine $\%CaCO_3$, while my study utilized coulometry. Between 14.5 and 25 ambsf (Core 3H), the bomb and coulometry data sets overlap and show good correlation ($R^2 = 0.79$) (Fig. 9).

The color reflectance records were interpolated at a 25 cm step (the coarsest sampling interval) to create the common depth scale needed for multiple linear

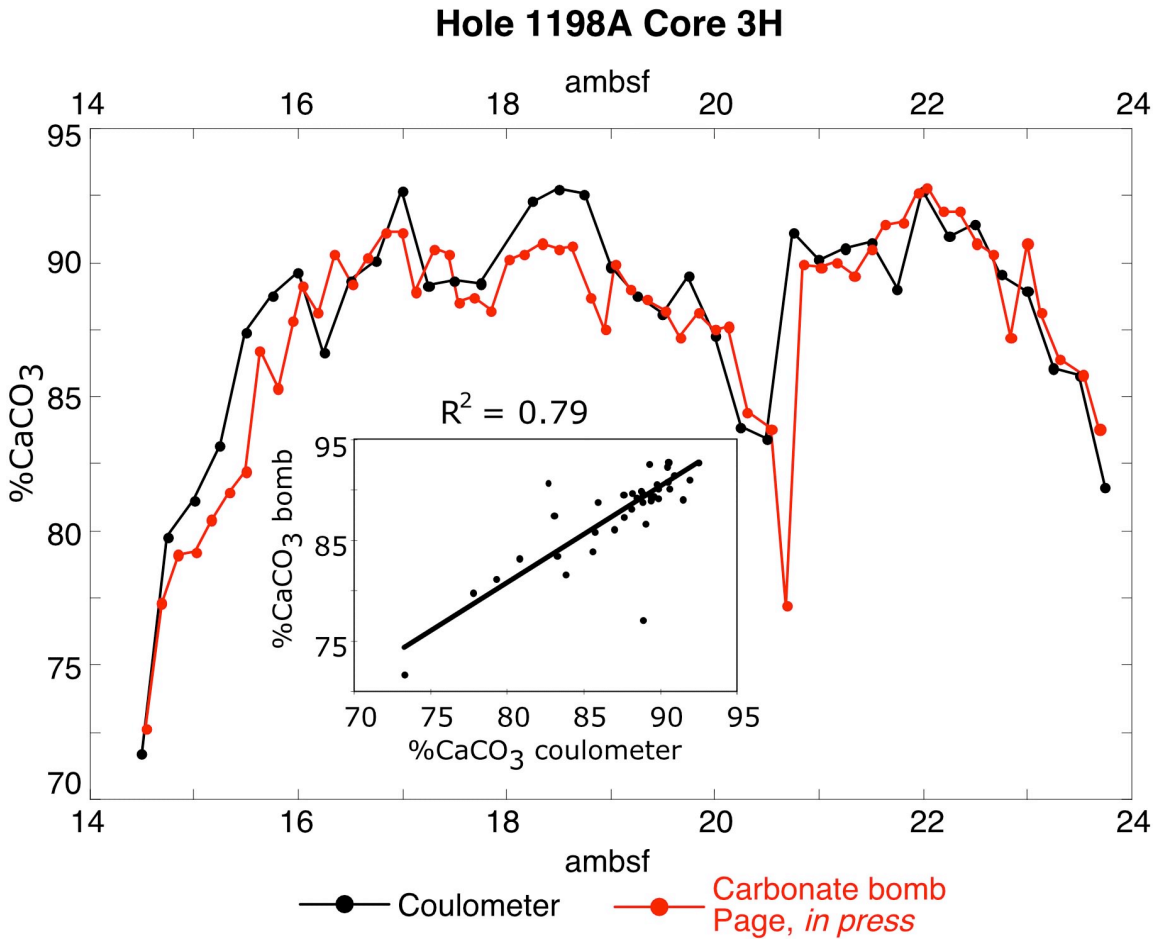


Fig. 9. Comparison of the carbonate bomb $\%CaCO_3$ data of Page (*in press*) (red) to that of this study (black) in Core 3H. Correlation coefficient is 0.79. The major discrepancy is a drop in $\%CaCO_3$ recorded by the carbonate bomb, but not by the coulometer, at ~ 21 ambsf. This difference maybe due to different sampling intervals.

regression. Each reflectance spectrum consists of 30 discrete measurements of percent reflectance between 400 and 700 nm (i.e., the visible spectrum) at a 10 nm step. Values were averaged and the result labeled as the average of the center measurement (e.g., AVE 420 = [410 nm + 420 nm + 430 nm] / 3; AVE450 = [440 nm + 450 nm + 460 nm]) (Fig. 10), decreasing the degrees of freedom from 30 to 10. Additionally, core photographs were examined and data points from disturbed core tops were removed (Table 4). The two lower intervals, which are separated by ~ 20 m (Table 1) were spliced together and color reflectance data points were accordingly removed (Fig. 11).

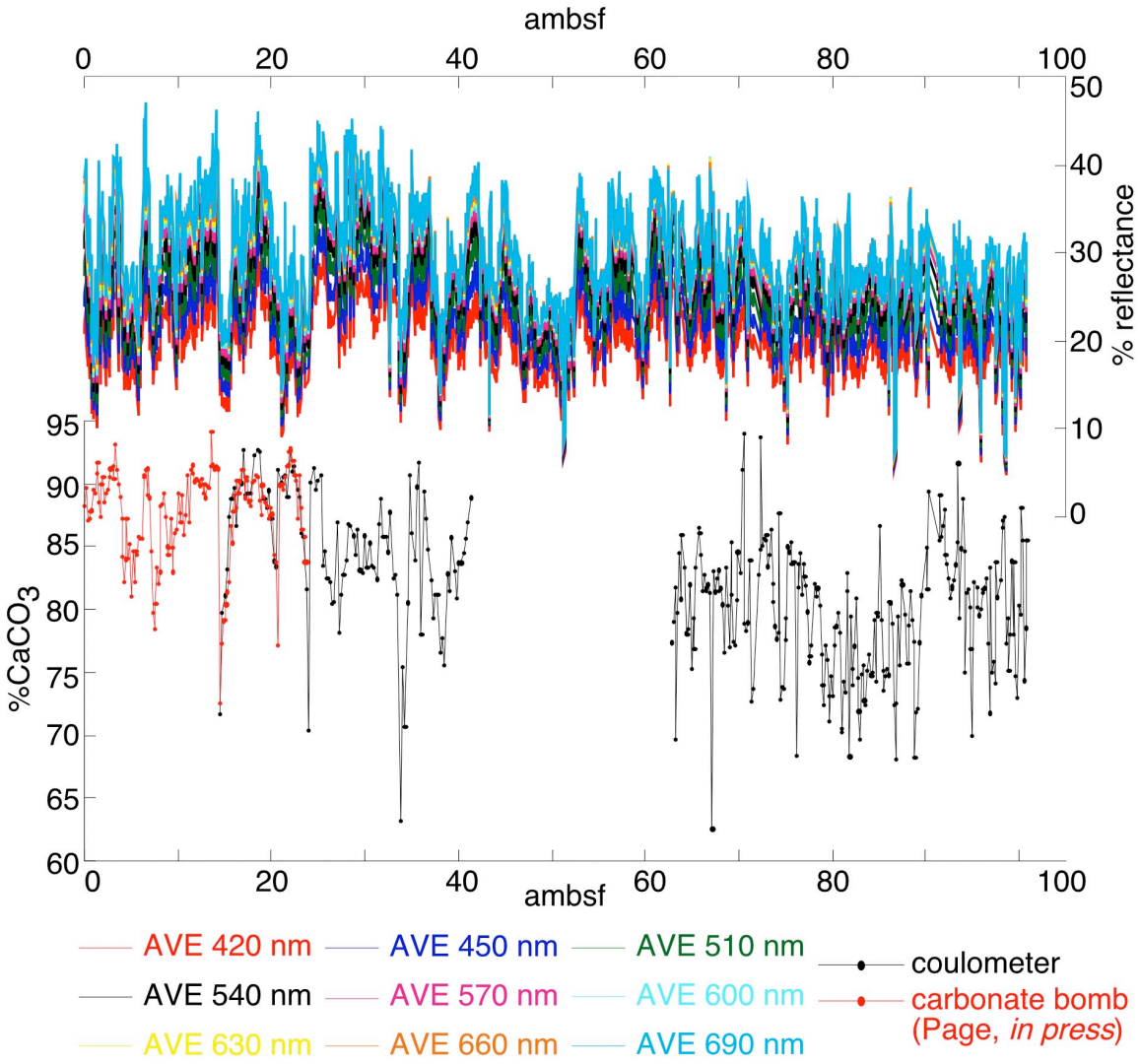


Fig. 10. %$CaCO_3$ data compared to raw color reflectance data after points in Table 3 were removed due to core-top disturbance. Coefficients determined by multiple linear regression were applied to raw color reflectance data to predict %$CaCO_3$ within the interval between 41.35 and 62.7 ambsf.

Percent $CaCO_3$ was interpreted from color reflectance data and calculated by the formula $Y = A + (\beta_{420}X_{420} + \beta_{450}X_{450} + \ldots + \beta_{690}X_{690})$, where Y is predicted %$CaCO_3$; X is % reflectance and $\beta$ is a coefficient, each at the subscripted wavelength; A is a constant (Millwood et al., 2002). The terms $\beta$ and A were determined by the regression. The resulting regression equation was applied to the raw, uninterpolated color reflectance data

| Core | Interval |
|---|---|
| 9H | 5 – 15 cm |
| 10H | 5 –25 cm |

Table 3. Intervals removed from color reflectance data due to core-top disturbance apparent in core photographs.

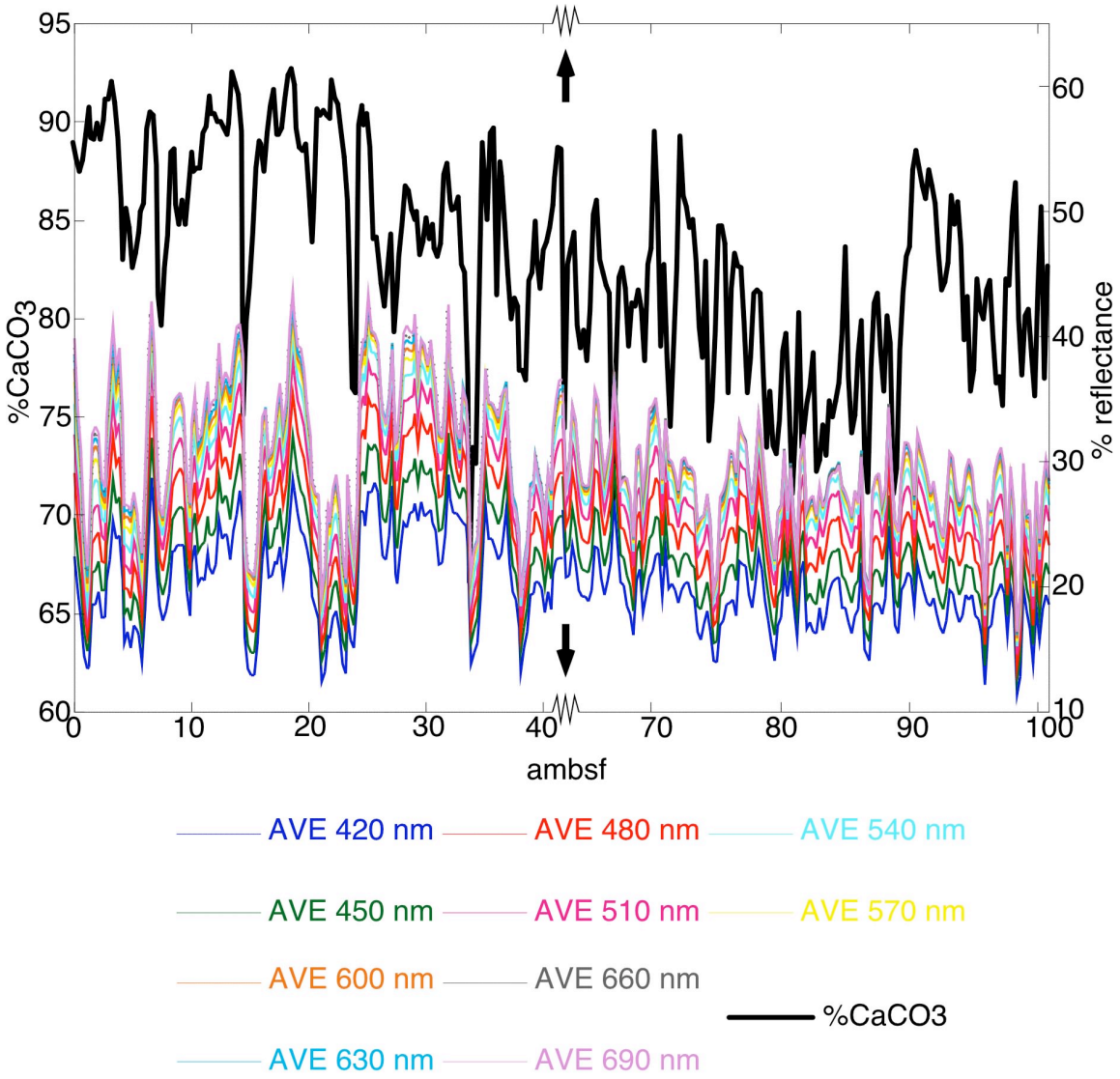


Fig. 11. Graphical depiction of data used in multiple linear regression. Page (*in press*) $\%CaCO_3$ from 14.5 ambsf to core top were spliced to $\%CaCO_3$ record of this study. The interval between 41.35 and 62.7 was removed from both the $\%CaCO_3$ and the color reflectance records. Arrows indicate where data are spliced. This is the domain and space used for the multiple linear regression. The color reflectance data have been resampled to the same depth scale as the $\%CaCO_3$ record.

from 0.05 to 100.85 ambsf to predict percent calcium carbonate through the entire upper 100 m of Hole 1198A.

## Mass Accumulation Rates

The mass accumulation rates (MAR; g/cm$^2$ k.y.) of ARA, HMC LMC, mud (< 63 $\mu$m), sand (> 63 $\mu$m), terrigenous (TER) were calculated using the formula, terrigenous MAR = LSR x DBD x P, where LSR, DBD, and P are linear sedimentation rate, dry bulk density, and the mass proportion of a particular component, respectively. LSR is determined from the compacted depth of sediment accumulated per unit time and typically expressed as cm/k.y. DBD was measured aboard ship once per 150 cm section of core, and this value was used in all MAR calculations for that respective section. The terrigenous mass proportion is the residual of the $CaCO_3$ content measurements (i.e., [100 - %$CaCO_3$] / 100). This assumption is based on XRD results and reflected light microscope observations of the sand fractions that indicate no significant authigenic non-carbonate components or biogenic silica and shipboard organic carbon measurements that averaged 0.05%. In addition, a TER MAR series was generated from the color reflectance data.

# RESULTS

## Oxygen Isotopes

*Globigerinoides ruber* $\delta^{18}O$ ranged between 0.11 and -1.79‰ PDB with an average standard deviation of 0.024‰ PDB (0.075 – 0.003‰ PDB range) (Fig. 6). Sampling frequency averaged 4.1 k.y., 3.4 k.y., and 3.9 k.y. for the Brunhes interval, Matuyama interval, and both intervals averaged, respectively.

## Lithology

XRD results indicate that, throughout Unit 1 of Hole 1198A, Aragonite (ARA), quartz (QTZ), low-Mg calcite (LMC), high-Mg calcite (HMC), and ankerite (Fe-rich dolomite) are present. Smectite, illite, kaolinite, and quartz were identified in the < 2$\mu$m fraction within both intervals. Siliceous sponge spicules are occasionally present. Microfossil tests are at times infilled by an unidentified, reddish-brown, authigenic material. Glauconite infilling of tests within the upper 30 m of Hole 1198A, as well as pyrite throughout, were reported (Shipboard Scientific Party, 2002), but no XRD peaks for glauconite, pyrite, or biosilica were present. Therefore, the noncarbonate fraction (i.e., residual of $\%CaCO_3$) is referred to as terrigenous material.

Pronounced glacial/interglacial-scale changes in the percentages of ARA, LMC, HMC, sand, and mud occur cyclically in the 100-k.y. world, Brunhes interval (Subunit 1A). LMC is the dominant carbonate mineral, ranging from 91% to 29% of the total carbonate content, while ARA and HMC percentages are 33% – 18% and 65% – 9%, respectively (Fig. 12). HMC and sand percentages peak during periods of rapidly decreasing $\delta^{18}O$ values. LMC and mud percentages are highest during periods of sustained low $\delta^{18}O$. ARA exhibits multiple peaks per Marine Isotope Stage, corresponding to periods of relatively rapid increasing and decreasing $\delta^{18}O$.

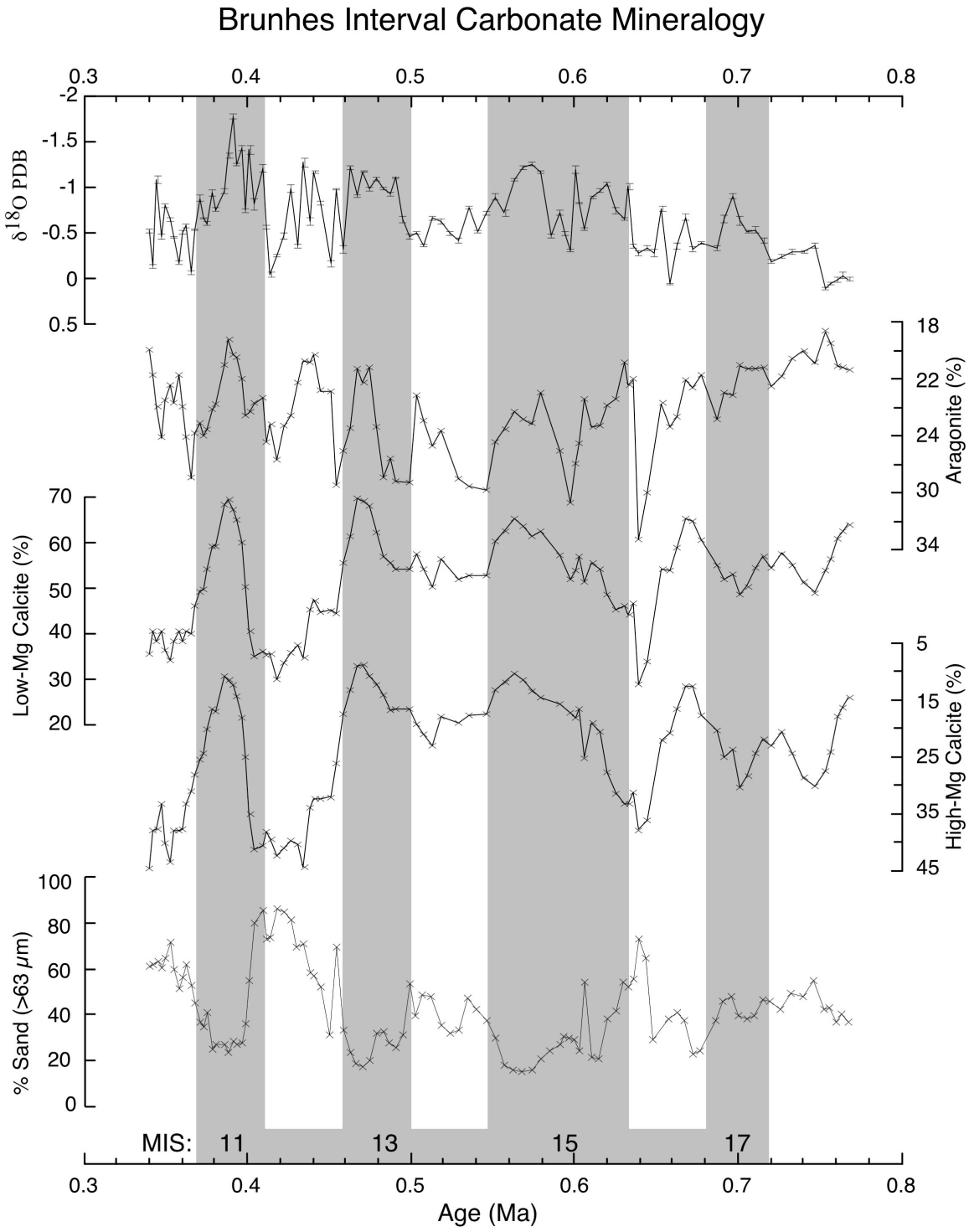


Fig. 12. Brunhes interval lithology, as determined by X-Ray diffraction analysis and sieving, compared to $\delta^{18}O$ record. Error bars on $\delta^{18}O$ record indicate analytical standard deviations. Shading denotes interglacial marine isotope stages. Note higher frequency variation of percent aragonite relative to that of low-Mg and high-Mg calcite. Low-Mg calcite percentages are highest during interglacial, while high-Mg calcite is highest during transgression.

LMC dominates the 41-k.y. world, Matuyama interval (Subunit 1B) (Fig. 13), which diagenesis severely affected. Percent ARA rapidly decreases in this interval from 20% at the top to < 5% at the bottom, rarely exceeding 10% below 70 ambsf. Likewise, LMC increases down-hole. Cyclic variations are superimposed on these trends. HMC ranges between 9% and 3%, averaging < 5% of the total carbonate and is, therefore, not detectable within the Matuyama interval (Subunit 1B).

Planktonic sediment, mainly comprised of foraminifers, dominates the sand (> 63$\mu$m) fraction throughout the sediment drift at Site 1198. In the entire Brunhes interval, whole planktonic pteropods and fragments are also common, as is neritic material, such as coral fragments, benthic foraminifera, bryozoans, red algae, and mollusks (Fig. 14a). The older, Matuyama subunit consists almost entirely of planktonic foraminifers. Neritic material is rarely present and pteropods are completely absent (Fig. 14b). Although the < 63 $\mu$m fraction was not optically examined, mud-sized fragments of calcareous green algae, such as *Halimeda*, probably contribute sediment to the drift.

Total percent calcium carbonate (%$CaCO_3$) varies cyclically between 94% and 63% of the total mass of sediment within the entire sedimentary succession (Fig. 15). A mean 2.5% difference and a range of 6.1% to 0.2% existed between duplicate analyses. Percentages of ARA, LMC, and HMC were normalized to the total carbonate present and reported as percent by mass of the total sediment (Fig. 16). Maximum percentages for ARA, LMC, HMC and terrigenous (TER) components was 30%, 82%, 56%, and 37%, respectively. The minimum value of LMC was 26%, while the other components had minima of approximate ≤ 5%. The highest percentage of terrigenous material corresponds to rapidly decreasing $\delta^{18}O$ values.

There is a significant correlation ($R^2 = 0.62$) between raw color reflectance data and measured %$CaCO_3$ at Hole 1198A (Fig. 17). Color reflectance data is, therefore, used to predict %$CaCO_3$ (Fig. 15). This model uses only 5 predictors, percent reflectance centered around 420, 450, 600, 630, and 690 nm. Using all 10 predictors resulted in a slightly higher correlation coefficient ($R^2 = 0.65$) due to the inclusion of insignificant predictors.

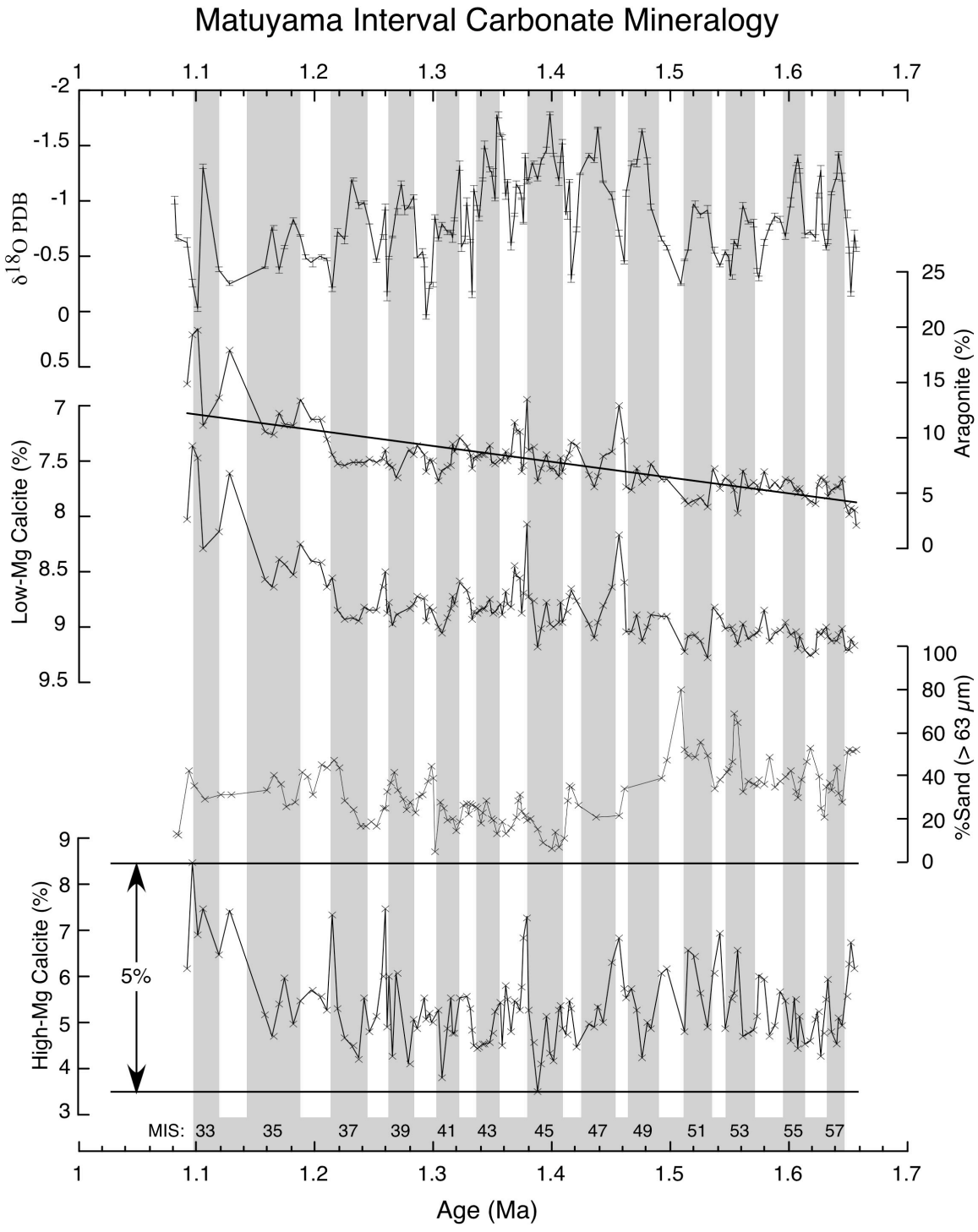


Fig. 13. Matuyama interval lithology, as determined by X-Ray diffraction analysis and sieving, compared to $\delta^{18}O$ record. Error bars on $\delta^{18}O$ record indicate analytical standard deviations. These sediments are strongly affected by diagenesis. Note the linear decrease of aragonite and the corresponding increase of low-Mg calcite . High-Mg calcite is not detectable.

# Hole 1198A Major Sediment Constituents

A

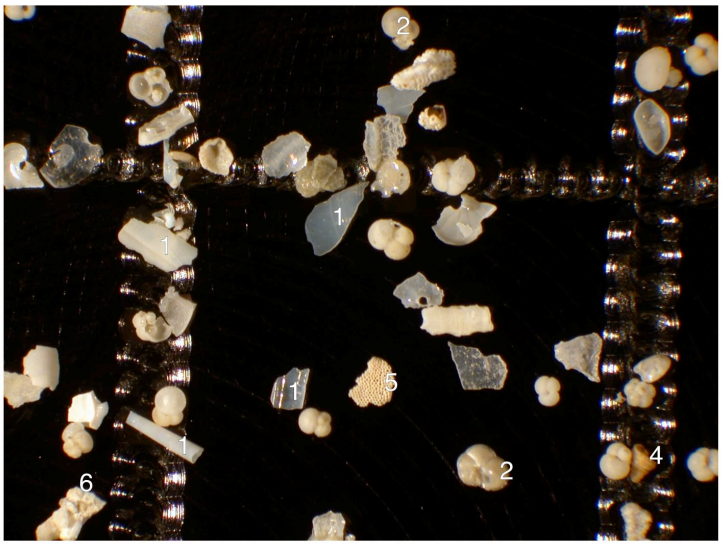


1 mm

ODP 194-1198A-4H-1W 0-4 cm
(> 355 μm, 24.0 ambsf; 0.45 Ma)

1. Pteropod fragments
2. Planktonic foraminifers
3. Coral (?) fragments
4. Neritic Mollusk
5. Bryozoan fragments
6. Unidentified neritic debris

B

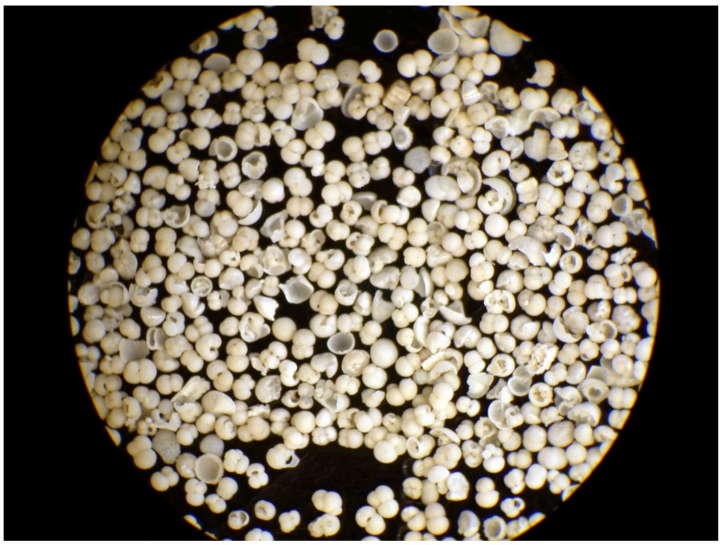

1 mm

ODP 194-1198A-10H-5W 125-129 cm
(> 355 μm; 89.0 ambsf; 1.48 Ma)

Fig. 14 A) Sample 1198A4H1W 0-4 cm (0.48 Ma), rich in pteropods and neritic debris (100-k.y. world interval; Subunit 1a of Shipboard Scientific Party, 2002). B) Sample 1198A10H5W 125-129 cm (1.48 Ma) is dominated by planktonic foraminfers (41-k.y. world interval; Subunit 1b of Shipboard Scientific Party, 2002).

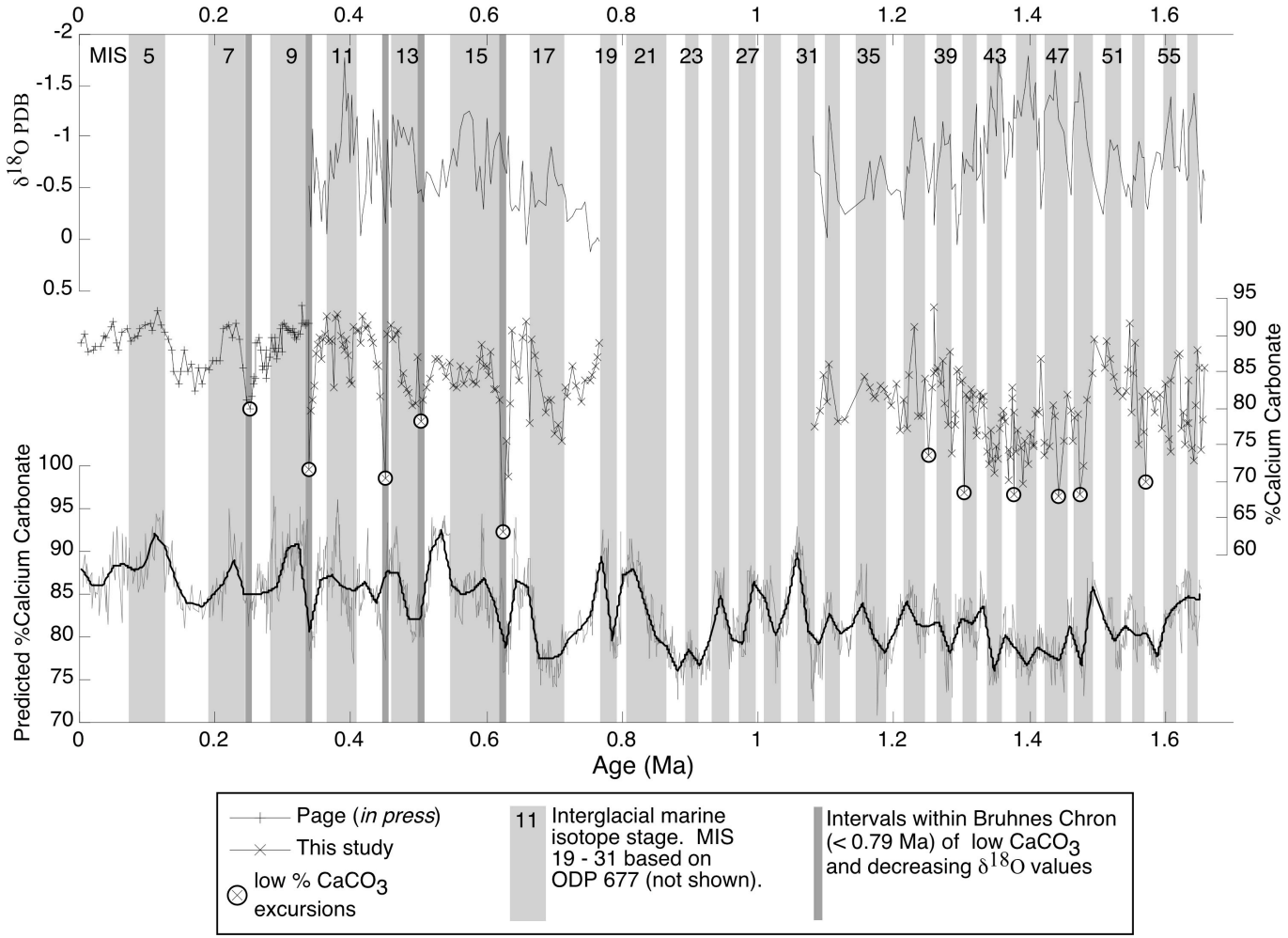


Fig. 15. Timing of low %$CaCO_3$ excursions illustrated with stable oxygen isotopes ($\delta^{18}O$), %$CaCO_3$, and predicted %$CaCO_3$. Light shading denotes interglacial marine isotope stages. Dark shading denotes correspondence between low %$CaCO_3$ excursions and decreasing $\delta^{18}O$ values within the Brunhes Chron (< 0.79 Ma). Note that low %$CaCO_3$ excursions within the Matuyama Chron (0.79 – ~ 2.5 Ma) do not correspond to $\delta^{18}O$ fluctuations.

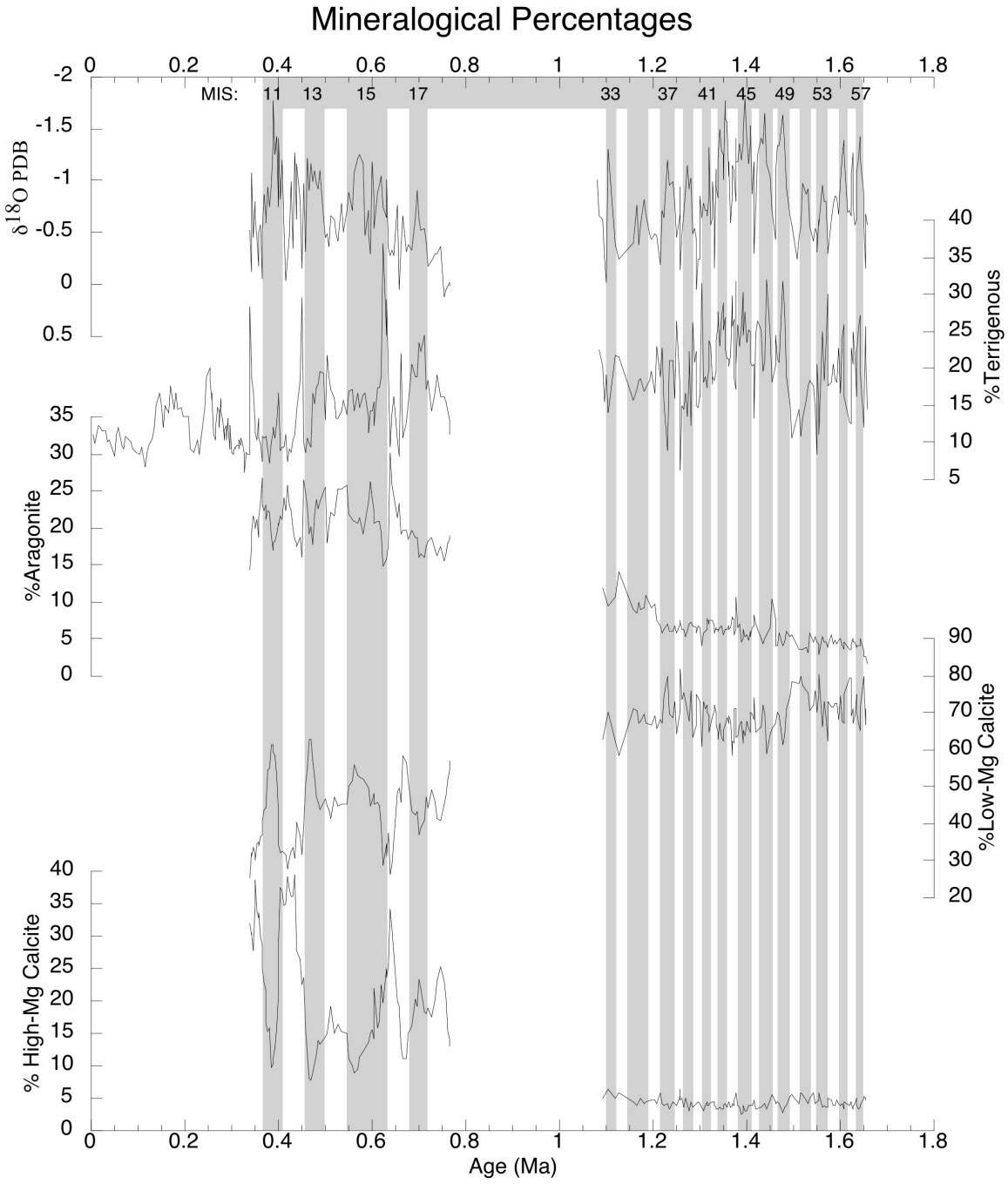


Fig 16. Carbonate mineralogy normalized to total %$CaCO_3$ to show percentages of terrigenous, aragonite, low-Mg calcite, and high-Mg calcite. Shading denotes areas of marine isotope stages.

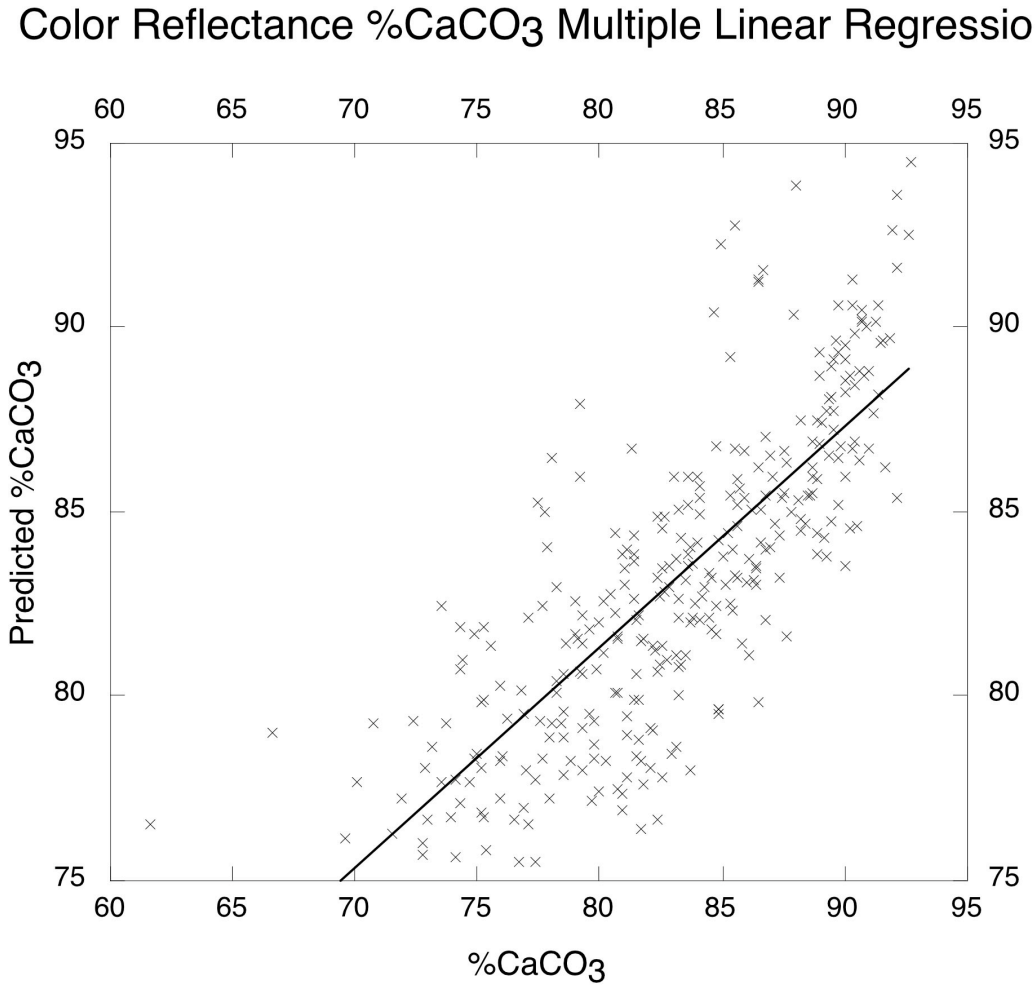


| | |
|---|---|
| $R^2$ | 0.62 |
| RMSE | 3.3 |
| Observations | 318 |
| F Ratio | 101.6 |
| Probablity > F | < 0.0001 |
| DF | 5 |

| Parameter | Estimate | Std. Error | t Ratio | Prob. > \|t\| |
|---|---|---|---|---|
| Intercept | 75.97 | 1.29 | 58.85 | <0.0001 |
| AVE 420 | -15.06 | 2.26 | -6.66 | <0.0001 |
| AVE 450 | 21.37 | 2.97 | 7.19 | <0.0001 |
| AVE 600 | -76.0 | 6.01 | -12.64 | <0.0001 |
| AVE 630 | 87.4 | 7.32 | 11.93 | <0.0001 |
| AVE 690 | -17.6 | 2.02 | -8.63 | <0.0001 |

Fig. 17. Results of multiple linear regression showing summary statistics, parameter estimations, and a scatter plot of measured versus predicted $\%CaCO_3$.

## Mass Accumulation Rates (MARs)

The MAR of each individual component is strongly correlated with its respective mineral percentage (Table 5) and influenced by DBD and LSR. In the Brunhes interval, MARs displays cyclic variation (Figs. 19 and 20) with a dominant 100-k.y. period (Fig. 21). HMC and sand MARs are well correlated ($R^2 = 0.90$) in the Brunhes Chron. Since at least 780 ka, TER, HMC, and sand MARs reach peak values during periods of rapid $\delta^{18}O$ decrease (Fig 19). LMC and mud MARs are also well correlated ($R^2 = 0.82$) in the Brunhes Chron, exhibiting highest values during periods of sustained low $\delta^{18}O$ (Fig 20). ARA peaks as $\delta^{18}O$ increases and decreases (Fig. 20).

The MAR of each individual component also has strong correlation with its respective mineral percentage in the Matuyama interval (Table 5). TER MAR does not clearly correspond to $\delta^{18}O$ variations but varies cyclically with periods of approximately 100, 41, and 18 k.y. (Fig. 21). Carbonate mineral MAR interpretations are complicated by diagenesis. ARA MAR variations are small, and superimposed on a linear decrease. LMC MAR remains elevated through much of the interval probably due to alteration of metastable ARA and HMC. LMC and mud MARs are not highly correlated ($R^2 = 0.33$) (Table 5). HMC MAR was not calculated as HMC was not significantly detectable by XRD analysis.

A TER MAR series was generated from core top to ~ 1.7 Ma by the residual of the predicted $\%CaCO_3$ record (Fig. 19). The assumption of a constant LSR from 0.770 to 1.1 Ma (Fig. 18) dampened variability within this interval. Significant power in this record exits at ~ 400, 100, and 40 k.y (Fig 21).

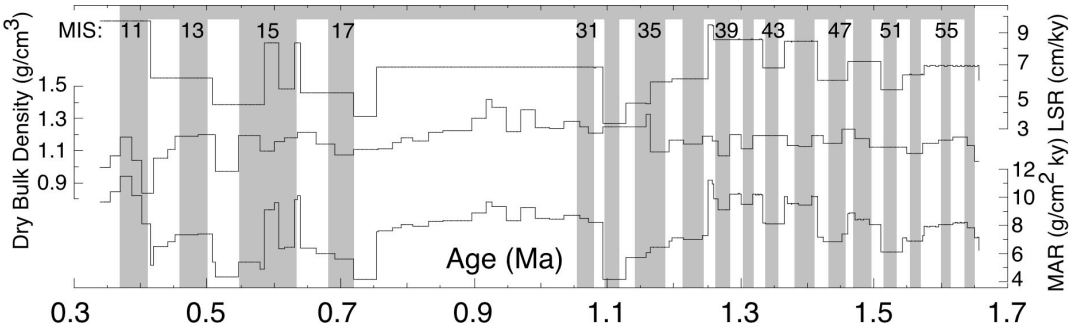


Fig 18. Bulk MARs calculated from dry bulk density (DBD) and linear sedimentation rate (LSR)

**Brunhes Interval**

| | %L | %H | %T | %S | %M | AMAR | LMAR | HMAR | TMAR | SMAR | MMAR | LSR | DBD | O-18 | |
|---|---|---|---|---|---|---|---|---|---|---|---|---|---|---|---|
| **%A** | 0.20 | 0.10 | 0.34 | 0.01 | 0.01 | 0.42 | 0.12 | 0.08 | 0.21 | 0.01 | 0.00 | 0.00 | 0.00 | 0.00 | **%A** |
| **%L** | 0.17 | 0.06 | **0.67** | **0.67** | 0.07 | 0.47 | 0.13 | 0.08 | 0.52 | 0.36 | 0.03 | 0.17 | 0.06 | **%L** |
| **%H** | 0.02 | **0.84** | **0.84** | 0.09 | 0.04 | **0.76** | 0.00 | **0.71** | 0.34 | 0.11 | 0.31 | 0.05 | **%H** |
| **%T** | 0.02 | 0.02 | 0.21 | 0.13 | 0.04 | 0.55 | 0.04 | 0.01 | 0.07 | 0.03 | 0.00 | **%T** |
| **%S** | **1.00** | 0.00 | 0.23 | 0.51 | 0.00 | **0.69** | 0.52 | 0.04 | 0.31 | 0.07 | **%S** |
| **%M** | 0.00 | 0.23 | 0.51 | 0.00 | **0.69** | 0.52 | 0.04 | 0.31 | 0.07 | **%M** |
| **AMAR** | 0.55 | 0.36 | 0.02 | 0.25 | 0.32 | **0.68** | 0.00 | 0.00 | **AMAR** |
| **LMAR** | 0.02 | 0.02 | 0.00 | **0.82** | 0.40 | 0.00 | 0.06 | **LMAR** |
| **HMAR** | 0.07 | **0.90** | 0.03 | 0.52 | 0.21 | 0.02 | **HMAR** |
| **TMAR** | 0.05 | 0.10 | 0.14 | 0.01 | 0.00 | **TMAR** |
| **SMAR** | 0.08 | 0.46 | 0.24 | 0.02 | **SMAR** |
| **MMAR** | 0.22 | 0.15 | 0.07 | **MMAR** |
| **LSR** | 0.13 | 0.01 | **LSR** |
| **DBD** | 0.00 | **DBD** |
| **O-18** | **O-18** |

| | %A | %L | %H | %T | %S | %M | AMAR | LMAR | HMAR | TMAR | SMAR | MMAR | LSR | DBD | |
|---|---|---|---|---|---|---|---|---|---|---|---|---|---|---|---|
| **%LMC** | 0.05 | **%A** | 0.20 | 0.10 | 0.34 | 0.01 | 0.01 | 0.42 | 0.12 | 0.08 | 0.21 | 0.01 | 0.00 | 0.00 | 0.00 | **%A** |
| **%HMC** | 0.18 | 0.55 | **%L** | 0.17 | 0.06 | **0.67** | **0.67** | 0.07 | 0.47 | 0.13 | 0.08 | 0.52 | 0.36 | 0.03 | 0.17 | 0.06 | **%L** |
| **%TER** | 0.06 | 0.03 | 0.00 | **%H** | 0.02 | **0.84** | **0.84** | 0.09 | 0.04 | **0.76** | 0.00 | **0.71** | 0.34 | 0.11 | 0.31 | 0.05 | **%H** |
| **%>63** | 0.05 | 0.21 | 0.25 | 0.15 | **%T** | 0.02 | 0.02 | 0.21 | 0.13 | 0.04 | 0.55 | 0.04 | 0.01 | 0.07 | 0.03 | 0.00 | **%T** |
| **%<63** | 0.04 | 0.00 | 0.03 | 0.17 | 0.06 | **%S** | **1.00** | 0.00 | 0.23 | 0.51 | 0.00 | **0.69** | 0.52 | 0.04 | 0.31 | 0.07 | **%S** |
| **AMAR** | **0.71** | 0.06 | 0.10 | 0.10 | 0.16 | 0.09 | **%M** | 0.00 | 0.23 | 0.51 | 0.00 | **0.69** | 0.52 | 0.04 | 0.31 | 0.07 | **%M** |
| **LMAR** | 0.01 | 0.48 | 0.12 | 0.03 | 0.00 | 0.04 | 0.22 | **AMAR** | 0.55 | 0.36 | 0.02 | 0.25 | 0.32 | **0.68** | 0.00 | 0.00 | **AMAR** |
| **HMAR** | 0.05 | 0.30 | 0.47 | 0.00 | 0.01 | 0.00 | 0.28 | 0.57 | **LMAR** | 0.02 | 0.02 | 0.00 | **0.82** | 0.40 | 0.00 | 0.06 | **LMAR** |
| **TMAR** | 0.00 | 0.06 | 0.16 | **0.75** | 0.27 | 0.18 | 0.12 | 0.09 | 0.02 | **HMAR** | 0.07 | **0.90** | 0.03 | 0.52 | 0.21 | 0.02 | **HMAR** |
| **SMAR** | 0.10 | 0.20 | 0.13 | 0.21 | **0.91** | 0.08 | 0.07 | 0.23 | 0.26 | 0.13 | **TMAR** | 0.05 | 0.10 | 0.14 | 0.01 | 0.00 | **TMAR** |
| **MMAR** | 0.00 | 0.07 | 0.14 | 0.12 | 0.07 | **0.77** | 0.19 | 0.33 | 0.09 | 0.40 | 0.00 | **SMAR** | 0.08 | 0.46 | 0.24 | 0.02 | **SMAR** |
| **LSR** | 0.01 | 0.05 | 0.01 | 0.09 | 0.06 | 0.10 | 0.18 | **0.71** | 0.39 | 0.45 | 0.00 | 0.45 | **MMAR** | 0.22 | 0.15 | 0.07 | **MMAR** |
| **DBD** | 0.17 | 0.17 | 0.11 | 0.11 | 0.00 | 0.16 | 0.14 | 0.01 | 0.08 | 0.07 | 0.08 | 0.05 | 0.08 | **LSR** | 0.13 | 0.01 | **LSR** |
| **O-18** | 0.00 | 0.00 | 0.01 | 0.06 | 0.01 | 0.24 | 0.02 | 0.02 | 0.00 | 0.09 | 0.00 | 0.19 | 0.06 | 0.00 | **DBD** | 0.00 | **DBD** |
| | **%A** | **%L** | **%H** | **%T** | **%S** | **%M** | **AMAR** | **LMAR** | **HMAR** | **TMAR** | **SMAR** | **MMAR** | **LSR** | **DBD** | **O-18** | | **O-18** |

**Matuyama Interval**

Table 5. Correlation coefficients ($R^2$) for percentages (%) and mass accumulation rates (MAR) of aragonite(A), low-Mg calcite (L), high-Mg calcite (H), terrigenous (T), sand-sized (S), and mud-sized (M) sediment. Values above 0.65 are in bold text. Upper portion is Brunhes interval. Lower portion is Matuyama interval.

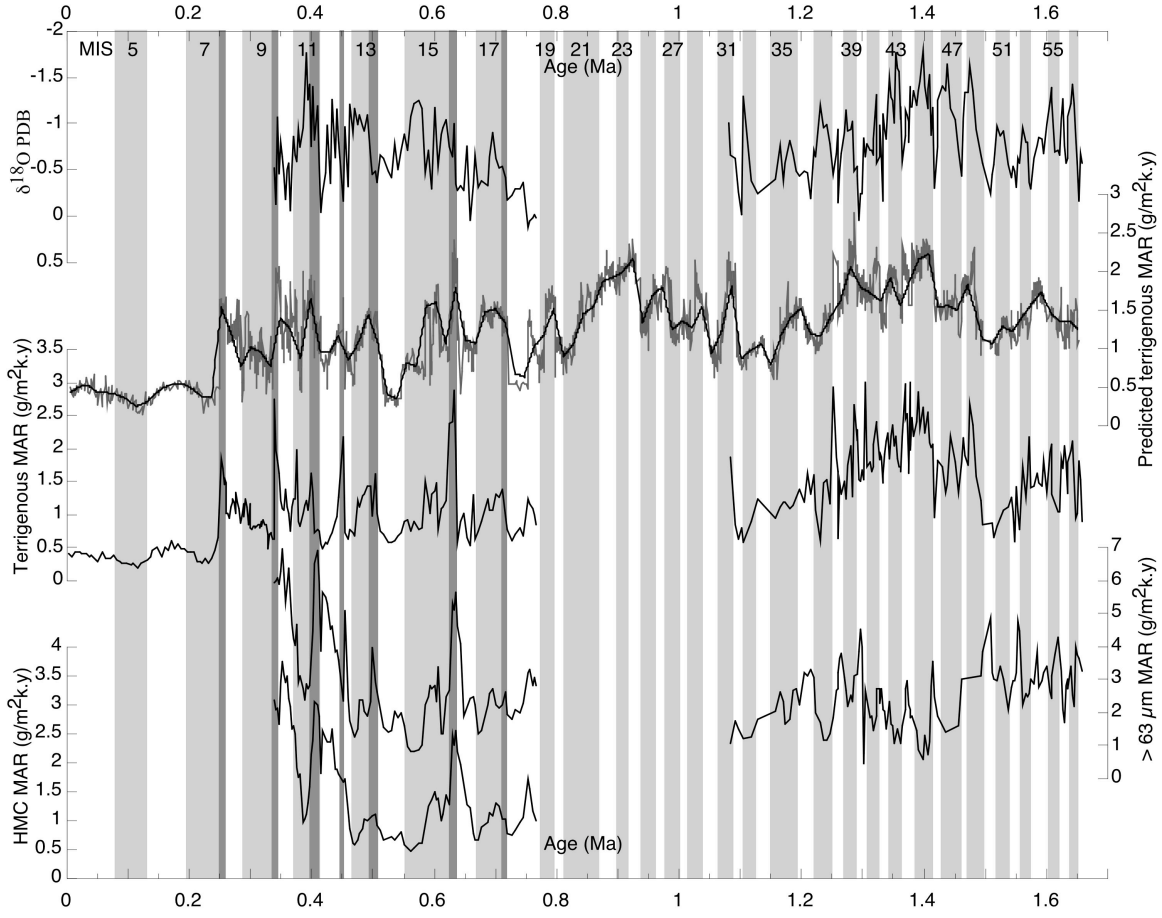


Fig. 19. Mass accumulation rates (MAR) of the sediment components that have the highest accumulation during sea-level transgression in the Brunhes Chron (< 0.79 Ma). Light shading denotes interglacial marine isotope stages. Dark shading denotes correspondence between excursions and decreasing $\delta^{18}O$ values. Note that in the Matuyama interval the highest terrigenous flux does not correspond to any particular phase of a marine isotope stage.

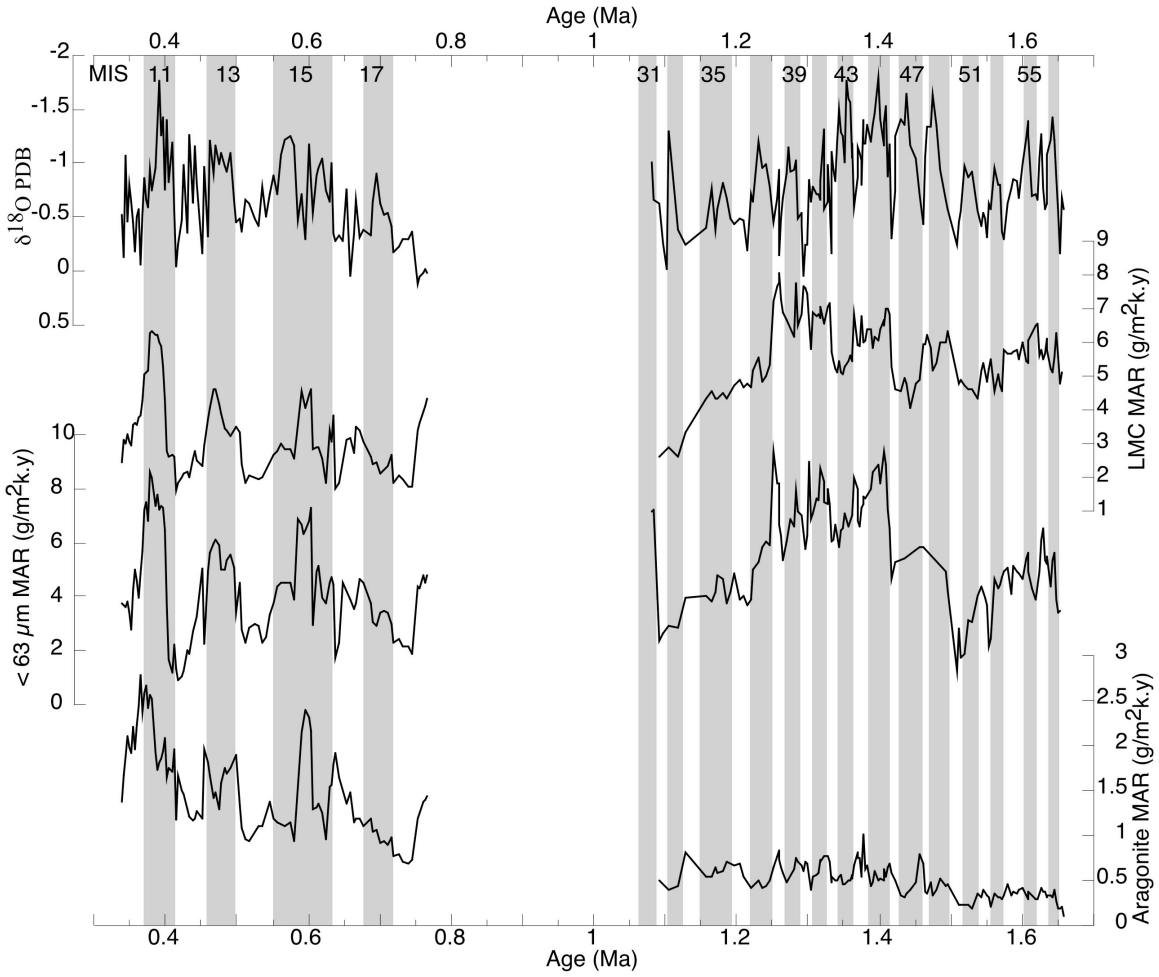


Fig. 20. Mass accumulation rates (MAR) of the sediment components that have the highest accumulation during sea-level highstand in the Brunhes Chron. Shading denotes interglacial marine isotope stages. Note that in the Matuyama interval the highest low-Mg calcite flux does not correspond to any particular phase of a marine isotope stage.

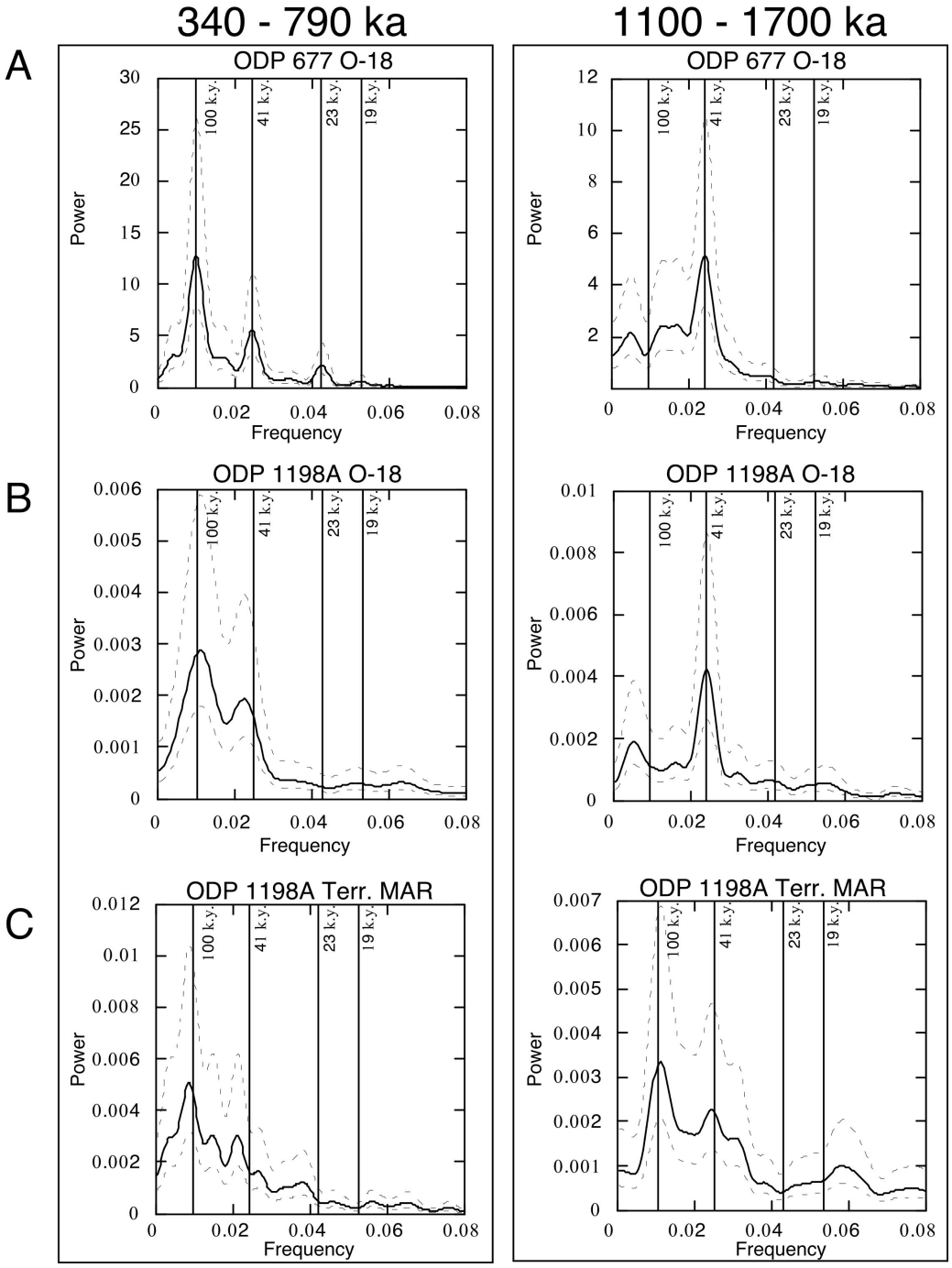


Fig 21. Spectral analyses from 340 to 790 ka and 1100 to 1700 ka. (A) Spectral analysis of ODP Site 677 $\delta^{18}O$, which was used to create the age model for Hole 1198A. Note the lack of precessional frequencies in the older interval. (B) Spectral analysis of Hole 1198A $\delta^{18}O$. Precession is not detectable in the oxygen isotope record of Hole 1198A. (C) Terrigenous MARs for Hole 1198A. Note that from 340 to 790 ka, TER MAR spectra correspond to corresponds to $\delta^{18}O$ spectra, indicating a response to eustacy. However from 1100 to 1700 ka, TER MAR spectra differ significantly from $\delta^{18}O$ spectra, indicating a response to factors other than sea-level fluctuations.

# DISCUSSION

## Sea-Level Fluctuations

The Marine Isotope Stages (MIS) identified in the Hole 1198A planktonic foraminifer $\delta^{18}O$ record exhibit the same overall shape and amplitude as those of the Site 677 benthic foraminifer record (Fig. 7). Therefore, the large amplitude variations (> 0.5‰) are interpreted to reflect eustacy, with decreasing isotopic values indicative of sea-level transgression and sustained low values indicative of sea-level highstand.

## Sediment Sources

The different lithologies represent sediment from different sources. Diagenesis is interpreted to have affected the entire sedimentary succession, but these affects are minimized in the younger, Brunhes interval, which, mostly retains its original mineralogy. HMC is primarily sand-sized, neritic material supplied by benthic foraminfers, bryozoans, and calcareous red algae (Fig. 22). LMC is primarily pelagic sediment, supplied mainly by planktonic foraminifers (Fig. 23). ARA represents a mixed source (Fig. 24). Increased ARA flux during sea-level transgression in the Brunhes interval likely represents increased neritic carbonate flux, while increased pelagic pteropods accumulation may account for other ARA MAR peaks.

Alteration of ARA and HMC to LMC in the older, Matuyama interval has resulted in high sustained of LMC (Fig. 20). The absence of pteropods may be due to mechanical destruction and/or diagenesis. The linear trend of decreasing aragonite in the 41-k.y. world interval indicates diagenesis (Fig. 13). ARA MAR fluctuations, although small, occur with decreased frequency relative to the younger interval, reflecting the absence of pteropods. In general, ARA and HMC MARs are expected to be lower prior to GBR initiation, a huge source of neritic carbonate.

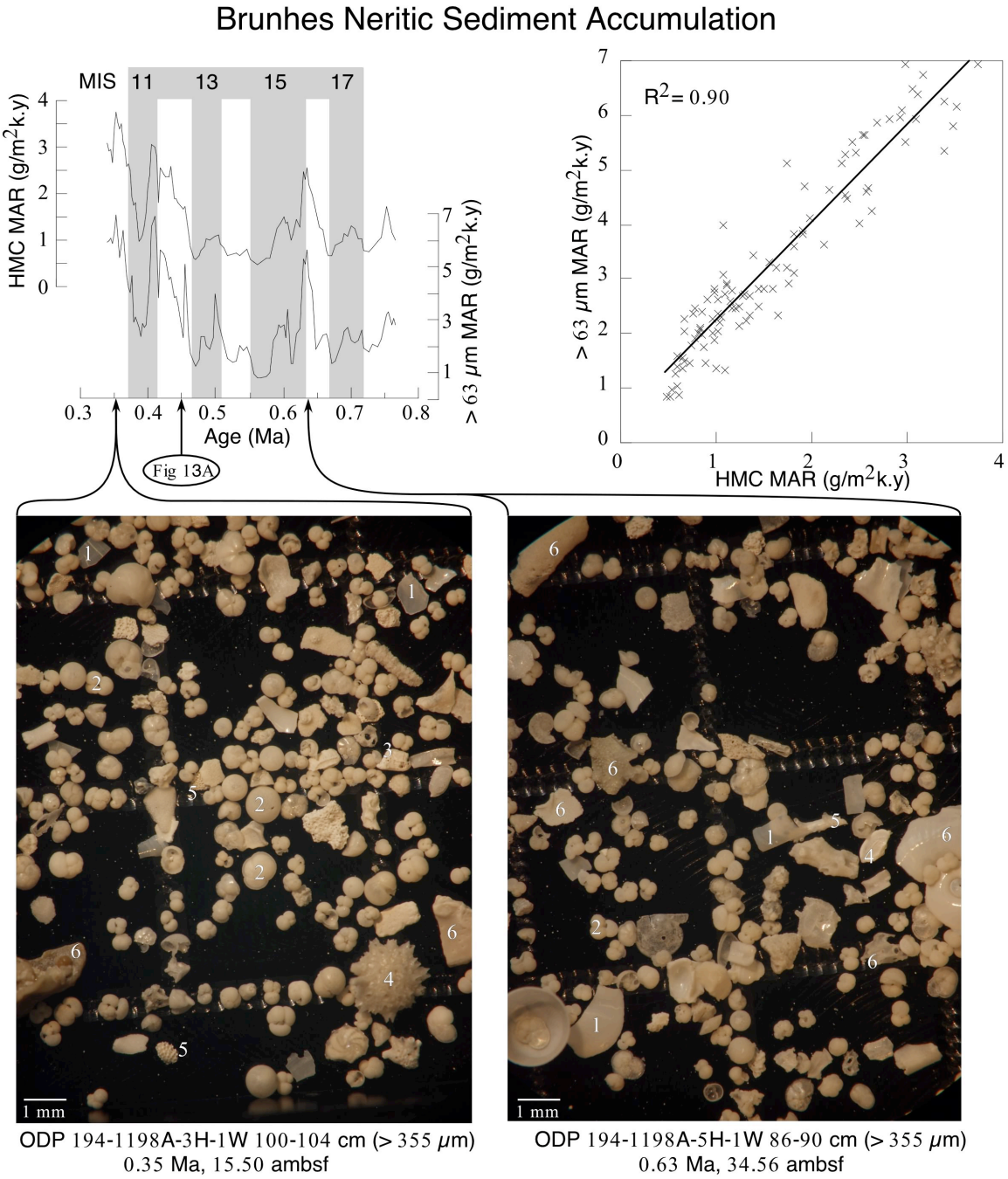


Fig. 22. Neritic sediment flux during the Brunhes Chron occurs primarily during sea-level transgression. Based on the correlation with HMC, the shed neritic material is primarily sand-sized. Benthic foraminifers, bryozoans, and calcareous red algae are predominantly HMC. Qualitatively, neritic sediment is more common within these intervals.

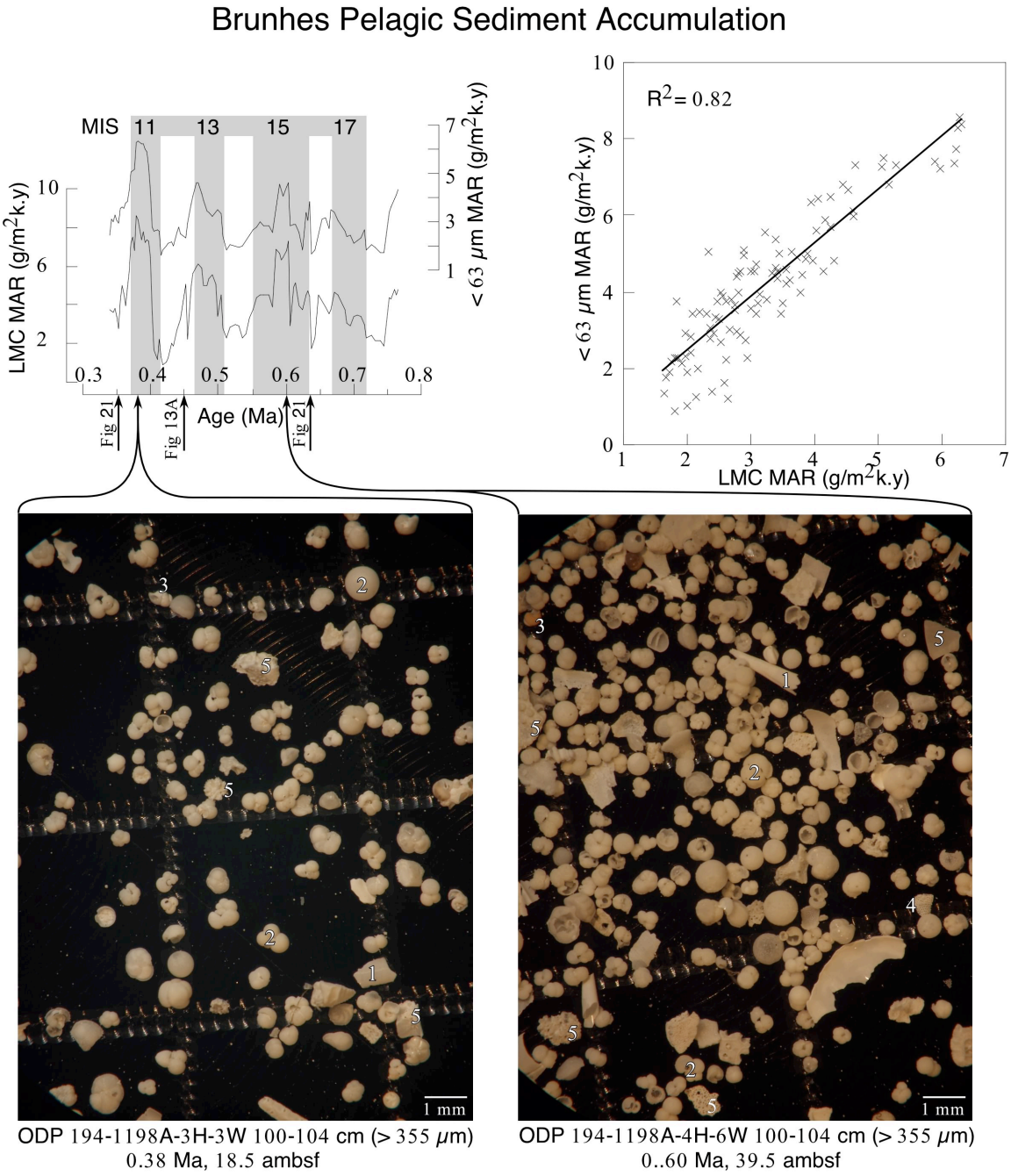


Fig. 23. Pelagic sediment flux during the Brunhes Chron occurs primarily late in a sea-level highstand. Qualitatively, pelagic sediment, primarily comprised of LMC dominates these intervals. The correlation between mud-sized sediment and LMC may reflect reduced current speed during highstand and/or diagenetic alteration of ARA and HMC sediments to LMC with an associated decrease in grain size.

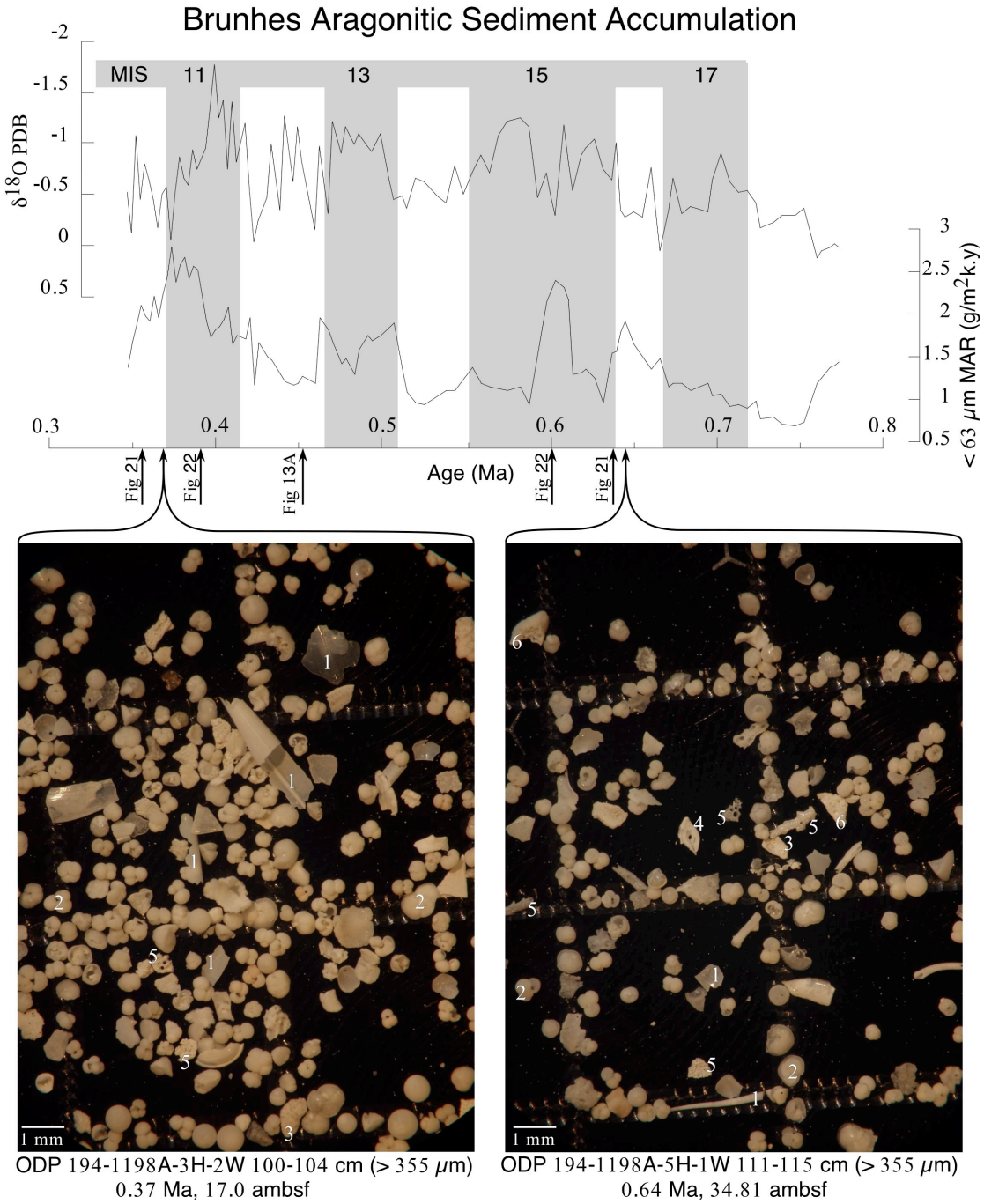


Fig. 23. ARA flues during late highstand correspond to pelagic pteropods, which are qualitatively more abundant during late highstand, while ARA fluxes during sea-level transgression is probably a result of neritic sediment shedding.

## Sediment Drift Architecture

The sediments comprising the drift at Hole 1198A have likely been transported some distance, as sand-sized skeletal fragments are common (e.g., Figs. 14, 22, 23, and 24). Nonetheless, the recognition of marine isotope stages with an expected amplitude and shape indicates this slumping is indeed minor and limited, with currents typically not reaching speeds high enough to significantly rework the planktonic foraminifer sand from with the oxygen isotope stratigraphy was generated. As the main path of the EAC is delflected around the Marion Plateau (e.g., Burrage et al., 1996), current speeds fall into the range of values critical for fine sediment deposition, allowing for the development of sediment drifts. This is the same mechanism attributed to the formation of Antarctic continental shelf sediment drifts (Harris et al., 1999; Harris et al., 2001)

### 41-k.y. World (Matuyama Interval)

Sediment drift architecture does not clearly correspond to the cyclic, 41-k.y. sea-level fluctuations characteristic of the early Pleistocene. TER, LMC, ARA, sand, and mud MARs peaks occur during all phases of a sea level cycle (i.e., transgression, highstand, regression, and lowstand; Figs. 18 and 19). Cyclic fluctuations are present, however. Spectral analysis of the TER MAR record, which is least, if at all, affected by diagenesis, revealed frequencies near those of the orbital parameters (i.e., eccentricity, obliquity, and precession) (Fig. 21B). The presence of all three orbital parameters cannot be solely explained by either eustatic sea-level fluctuations or local insolation variations, implying contribution from both global sea level and local climate to the cyclic lithological sedimentary architectural changes.

Eustatic sea-level fluctuations account for the 41 k.y. power in the TER MAR record, while the presence of near-precessional frequencies may be the result of local insolation variations forcing monsoon-like precipitation on a precessional timescale. Qualitatively, TER, LMC, sand and mud MARs often peak twice per 41-k.y. sea-level

cycle. The power at the 100-k.y. period may result from eccentricity's modulation of precession.

The early Pleistocene, pre-MPCT, northern-hemisphere ice sheets waxed and waned with a 41 k.y. period (obliquity) without significant contribution from eccentricity (100 and 413 k.y.) and precession (19 and 23 k.y.), as reflected by the ODP Site 677 benthic foraminifer $\delta^{18}O$ record (Fig. 21a). However, obliquity does not affect insolation at the equator (e.g., Laskar, 1990). The Marion Plateau is located at 20° S latitude, where obliquity affects are minimal and summer insolation is out of phase with that of the northern hemisphere (Fig. 25). Therefore, a locally generated climatic signal may produce a lithological response that is out of phase with that generated by sea level, perhaps explaining why MAR peaks do not correspond to a particular phase of a sea-level cycle. Based on the amplitude of $\delta^{18}O$ variations, it is reasonable to assume that sea-level variations were also of a lower amplitude in the early Pleistocene than in the late Pleistocene. These lower-amplitude sea-level cycles may have allowed for a greater expression of local climate forcing.

## Mid Pleistocene Climate Transition

During the MPCT, sea level appears to have exerted a larger control on the architecture of the sediment drift than in the early Pleistocene. Variations in percent $CaCO_3$ interpreted from color reflectance data correspond remarkably to the Marine Isotope Stages of ODP Site 677, primarily exhibiting one peak and one trough per sea-level cycle (Fig. 7). Although there is no direct age or sea-level control (i.e., $\delta^{18}O$), troughs in percent $CaCO_3$ tend to correspond to sea-level lowstand, which is suggestive of reciprocal sedimentation (Fig. 2), in which the highest off-shelf flux of carbonate and terrigenous sediments occurs during sea-level highstand and lowstand, respectively. Mass accumulation rates do not exhibit this relationship to Marine Isotope Stages due to dampening caused by an assumed, constant linear sedimentation rate.

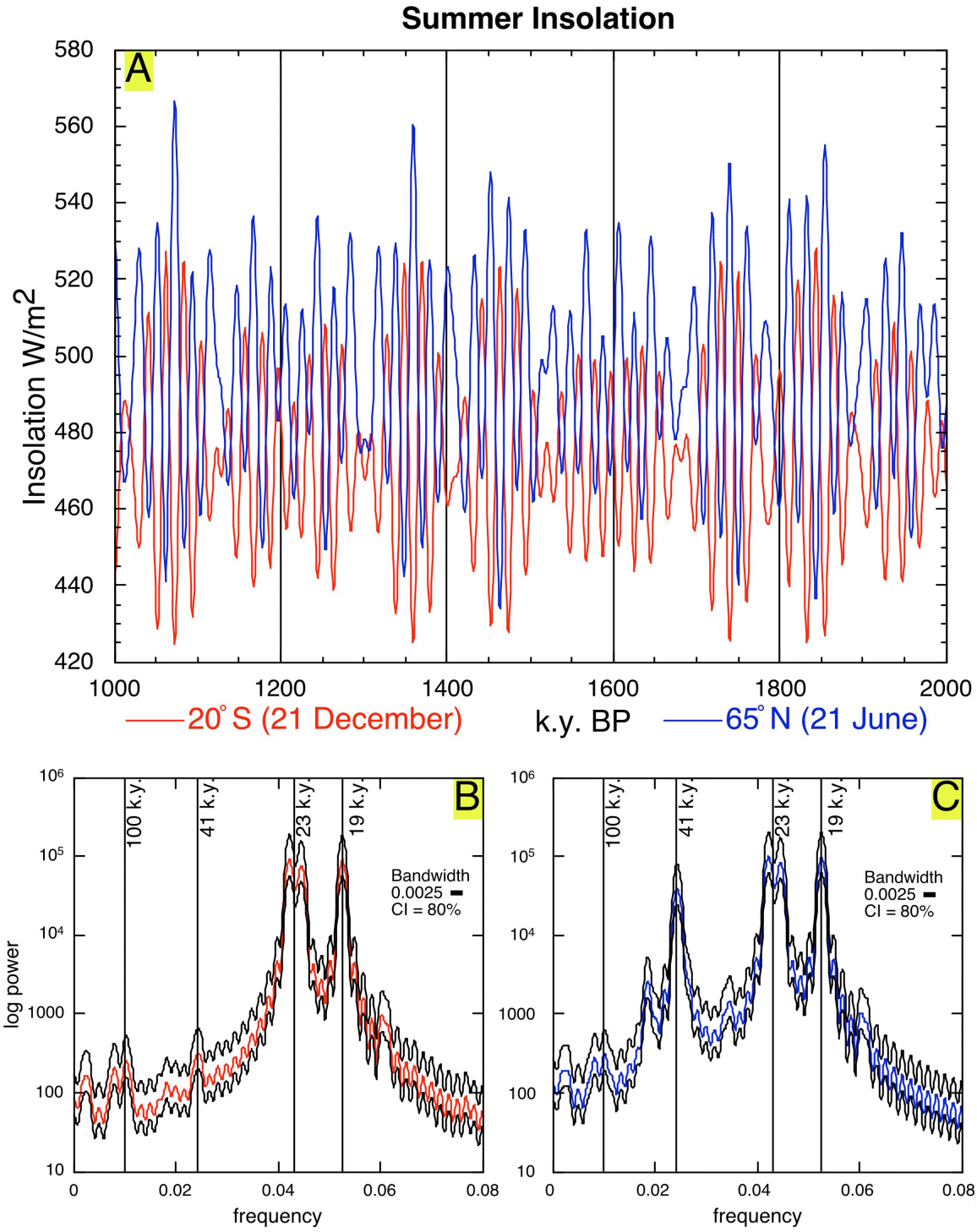


Fig. 25. A) Comparison of 41-k.y. world, summer insolation at 65° N latitude, which controls the growth and decay of northern hemisphere ice sheets (i.e., eustatic sea level), and that of 20° S latitude where the Marion Plateau is located. Note sea-level and local forcing are out of phase. B and C) Obliquity (41 k.y.) is not expressed in the spectral analysis of 20° S insolation (B) but is expressed in that of 65°N. The power at 41-k.y. in the TER MAR record cannot be produced locally, but must be a response to eustacy.

100-k.y. World (Brunhes Interval)

Eustatic sea-level cyclicity clearly controls the post-MPCT sedimentary architecture of this shallow water drift (Fig. 19). Terrigenous and neritic sediment-rich layers correspond to increased flux of these components during sea-level transgression This is reflected by peaks at glacial terminations of TER MAR, HMC and sand, and ARA. The highest accumulation of pelagic sediment occurs during sea-level highstand, and to a lesser extent, regression. The high correlation between increased LMC and mud MARs may be a result of diagenetic alteration of ARA and HMC to LMC with an associated decrease in particle size. This relationship may be enhanced by decreased EAC current speed during interglacial periods allowing for increased accumulation of mud-sized pelagic LMC such as coccolith plates.

This architecture indicates a rimmed shelf morphology existed within the entire upper interval of Hole 1198A. Without a rimmed shelf, high terrigenous sediment slope sedimentation would occur at sea-level lowstand (Fig 2) (Dunbar et al., 2000; Dunbar and Dickens, 2003a; b; Page et al., 2003; Page, *in press*). The higher amplitude $\delta^{18}O$ excursions of the 100-k.y. world are probably due to higher magnitude sea level fluctuations, which could also serve to strengthen the response of off-shelf sedimentation to sea level. The effects of local climate, such as variations in precipitation amount, do not produce a noticeable signal in the sediment drift architecture. Precipitation during the most recent sea-level cycles increased during interstadials and interglacials (Kershaw and Nanson, 1993; Kershaw et al., 2003), but sea-level and the presence of a barrier reef ultimately control the delivery of this material to the sediment drift.

## Initiation of the Great Barrier Reef

The Australian, Belize, and Florida barrier reefs were initiated post-MPCT in a changed glacial world, characterized by saw-toothed, increased amplitude glacial/interglacial sea-level cycles that eventually developed a 100 k.y. period. Evidence also exists for globally increased sea-surface temperatures during sea-level highstands in

the mid Brunhes (Kroon et al., 2000). Perhaps one or more of these changes created conditions conducive to reef growth. One plausible explanation is that higher sea level, coupled with increased sea surface temperature, reflooded previously exposed outer continental shelves and isolated platform tops during MIS 11, creating, perhaps for the first time since the onset of Late Cenozoic northern hemisphere glaciation, habitat suitable for shallow-water, reef-building corals (Droxler et al., 2003a). This is supported by Sr isotope data that indicate an age of 600 ± 280 ka on material taken from the base of the Ribbon Reef 5 borehole though the outer central GBR (International Consortium, 2001). After further analysis of this core, 365 – 452 ka (MIS 11) was proposed as the period for initiation of the outer reef section within the central GBR (Webster and Davies, 2003). In addition, Braithwaite et al. (2004) concluded that no significant barrier reef existed prior to MIS 11 in this location.

However, interpretation of the off-shelf flux of terrigenous sedimentation in the context of existing NE Australia sedimentation models (Dunbar et al., 2000; Dunbar and Dickens, 2003a; b; Page et al., 2003), indicates that a rimmed platform morphology probably developed prior to MIS 11 in the south central GBR region. The GBR is interpreted to be progressively younger from north to south (Davies et al., 1989), so it is unlikely that the a rim developed significantly earlier in the south central GBR than the central GBR. A major flux of terrigenous sediment occurred during sea level transgression at the onset of MIS 15 within the Marion Plateau sediment drift (Fig. 19). This indicates that sediment accumulated behind a barrier during the sea-level lowstand of MIS 16. Initiation of the GBR likely created this barrier during a previous highstand of sea level.

The first true, shallow-water, high-energy coral reef growth occurred from ~ 135 to ~ 115 mbsf in the 210-m long Ribbon Reef 5 borehole (Webster and Davies, 2003) (Fig. 26). I propose this section created the barrier responsible for the large flux of terrigenous material during the termination of MIS 16. The entire Ribbon Reef 5 borehole exhibits normal paleomagnetic polarity, indicating the base cannot be older than the Brunhes-Matuyama boundary (780 ka) (International Consortium, 2001).

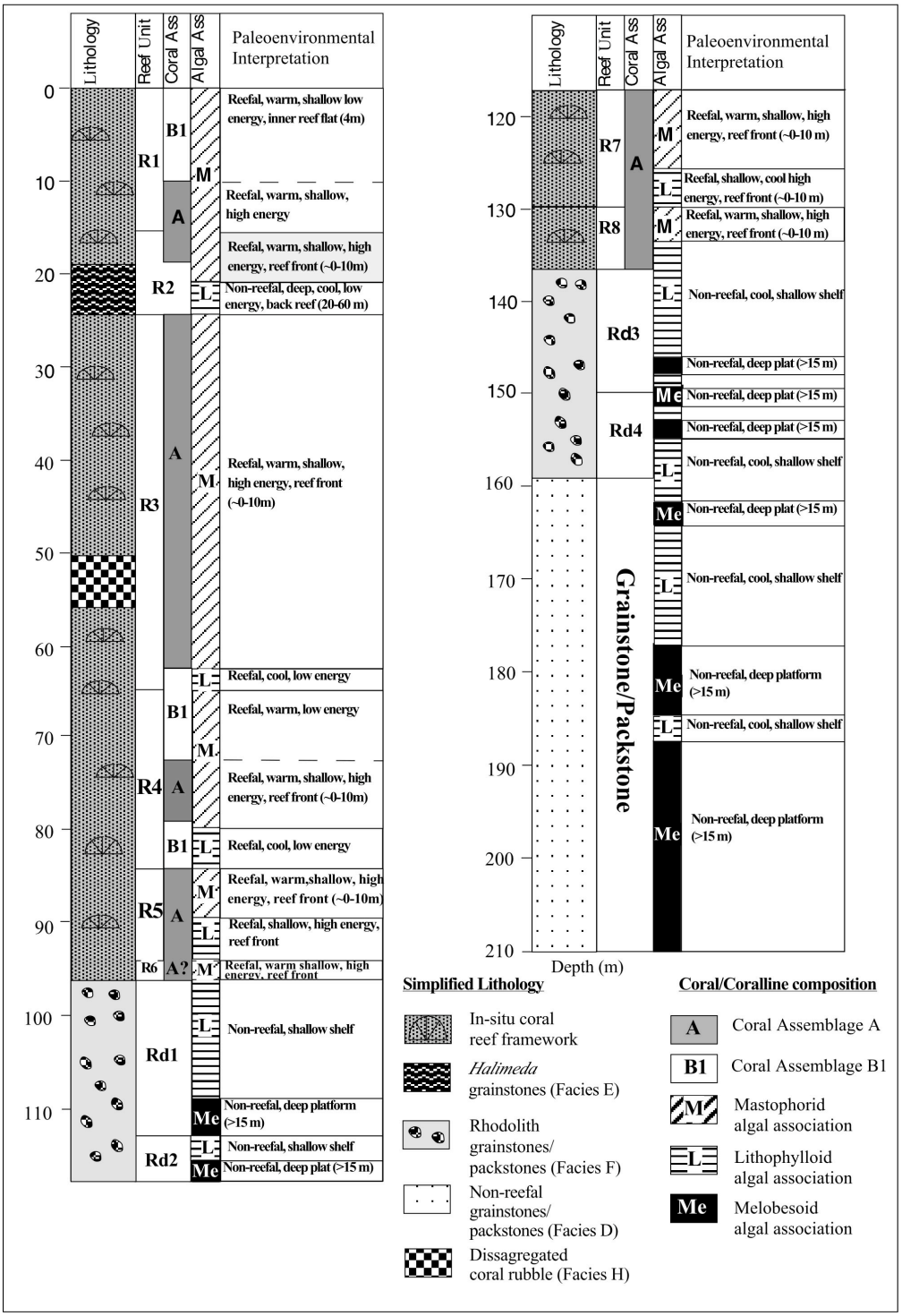


Fig. 26. Lithologic interpretation of the Ribbon Reef 5 borehole (Fig. 6 of Webster and Davies, 2003). Coral reef facies at ~ 135 mbsf is herein proposed to correspond to GBR initiation during MIS 17. Reef growth was not continuous as indicated by rhodolith facies. Reinitiation of coral reef growth probably occurred during MIS 11.

Underlying the initial 20-m section of coral reef is a ~ 20-m thick rhodolith facies, in turn underlain by a ~55-m thick grainstone/packsone facies. It is unlikely that these facies produced the needed relief to prevent significant lowstand, off-shelf sedimentation (J. Webster, personal communication, 2004).

I also propose that the initial coral growth at ~ 135 mbsf in the Ribbon Reef 5 borehole occurred during MIS 17. The preceding highstand of MIS 19 contained the Brunhes-Matuayama boundary, which significantly predates GBR initiation based on the normal magnetic polarity of the borehole. After Pleistocene glacial ice volume increased beginning with MIS 22 during the MPCT, MIS 17 was the first of the sawtoothed, high amplitude sea-level cycles of the 100-k.y. world. Prior to MIS 17, the NE Australia margin A second rhodolith facies (~ 115 to ~95 mbsf) overlies the initial coral reef section. This reef shut-down phase probably corresponds to the intermediate climatic conditions of MIS 14 and MIS 13. From ~95 mbsf, the borehole exhibits a continuous coral reef facies. This reef "turn on" probably occurred during MIS 11 (Webster and Davies, 2003). The above-mentioned scenario is summarized in Fig. 27.

## Implications for Globally Synchronous Reef Initiation

Perhaps the Florida Keys and Belize barrier reefs were not initiated during MIS 11. The timing of initiation of the Belize barrier reef is based solely on biostratigraphic datum levels (Droxler et al., 2002), while the basal carbonates of the Florida barrier reef have yet to be dated (Multer et al., 2002). Although barrier reefs world-wide have certainly flourished post-MIS 11, perhaps this was not a period of global reef initiation. Without better chronologies for the Florida and Belize barrier reefs, whether the Pleistocene reef-initiation events were indeed synchronous will remain unknown. Synchronous barrier reef initiation in the southern and northern hemispheres would imply that global factors were more important than regional or hemispheric environmental conditions.

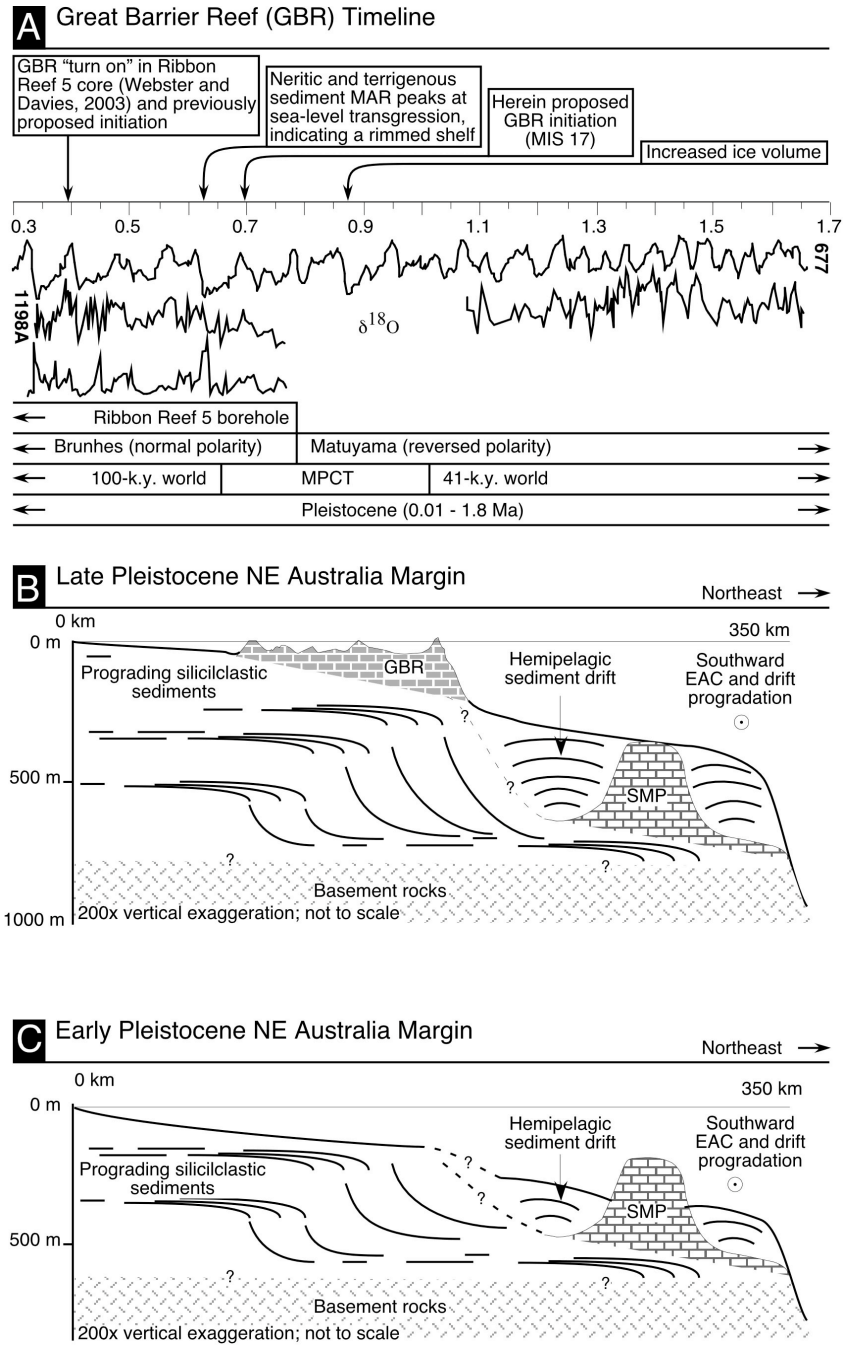


Fig. 27. A) Timeline of the Great Barrier Reef. From MIS 22, during the MPCT, continental ice volume increased, and by MIS 17, Marine Isotope Stages became asymmetric in shape. A massive pulse of terrigenous material during the sea-level transgression of MIS 15 indicates siliciclastic sediment accumulated behind a barrier reef during the lowstand of MIS 16. This and the normal polarity of the Ribbon Reef 5 borehole (International Consortium, 2001) constrains the timing of GBR initiation to MIS 17. B) Late Pleistocene cross section through NE Australia margin showing GBR location and buried carbonate platforms. C) The early Pleistocene NE Australia margin lacked a barrier reef. Drowned carbonate platforms cropped out of the sea floor.

# CONCLUSIONS

Great Barrier Reef (GBR) initiation during MIS 17 is indicated by the sedimentary architecture of a shallow-water (< 500 m) hemipelagic sediment drift located seaward and downstream of the reef. A large pulse of terrigenous material to the drift occurred during the sea-level transgression of MIS 15 due to the accumulation of siliciclastic material behind a barrier reef during the previous sea-level lowstand. The normal polarity exhibited by the central GBR and thick section of underlying sediments indicates initiation occurred within the Brunhes Chron (780 ka to present), ruling out MIS 19 (International Consortium, 2001). The high-amplitude, asymmetric (sawtoothed) sea-level cycles began with MIS 17, but whether GBR initiation is related to a global or local events remains unknown. If the Belize and Florida Keys barrier reefs are indeed contemporaneous to the GBR, then global factors likely initiated reef growth.

Sediment drift architecture responded increasingly to sea-level fluctuations during the Pleistocene. In the early Pleistocene, local climatic variations introduced a precessional rhythm to drift architecture that was out of phase with sea level-forced cyclicity. From the mid Pleistocene, sea level variations dominated drift architecture. After Great Barrier Reef initiation, the drift exhibits a predictable sedimentary architecture, with the highest flux of terrigenous, neritic, and sand-sized sediment occurring during sea-level transgression as sediment trapped behind an exposed barrier reef is remobilized by rising sea level.

# REFERENCES


Andrews, J.C. and Clegg, S., 1989. Coral Sea circulation and transport deduced from modal information models. Deep-Sea Research Part a-Oceanographic Research Papers, 36(6): 957-974.

Andrews, J.C. and Furnas, M.J., 1986. Subsurface intrusions of Coral Sea-water into the central Great-Barrier-Reef 1: structures and shelf-scale dynamics. Continental Shelf Research, 6(4): 491-514.

Beach, D.K. and Ginsburg, R.N., 1980. Facies succession of Pliocene-Pleistocene carbonates, northwestern Great Bahama Bank. AAPG Bulletin-American Association of Petroleum Geologists, 64(10): 1634-1642.

Berger, W.H. and Jansen, E., 1994. Mid-Pleistocene climate shift: The Nansen connection. In: O.M. Johannessen, R.D. Muench and J.E. Overland (Editors), The polar oceans and their role in shaping the global environment: The Nansen Centennial volume Geophysical Monograph 85. AGU, pp. 295-312.

Boardman, M.R. and Neumann, A.C., 1984. Sources of periplatform carbonates - northwest Providence Channel, Bahamas. Journal of Sedimentary Petrology, 54(4): 1110-1123.

Boardman, M.R. and Neumann, A.C., 1986. Banktop responses to quaternary Fluctuations in sea-level recorded in periplatform sediments - reply. Geology, 14(12): 1040-1041.

Braithwaite, C.J. et al., 2004. The Great Barrier Reef: The chronological record from a new borehole. Journal of Sedimentary Research, 74(2): 298-310.

Burrage, D.M., Steinberg, C.R., Skirving, W.J. and Kleypas, J.A., 1996. Mesoscale circulation features of the Great Barrier Reef region inferred from NOAA satellite imagery. Remote Sensing of Environment, 56(1): 21-41.

Church, J.A., 1987. East Australian Current adjacent to the Great Barrier Reef. Australian Journal of Marine and Freshwater Research, 38: 671-683.

Davies, P.J., McKenzie, J. A., Palmer-Julson, A., et al., 1991. Proceedings ODP Initial Reports, 133. Ocean Drilling Program, College Station, TX.

Davies, P.J., Symonds, P.A., Feary, D.A. and Pigram, C.J., 1989. The evolution of the carbonate platforms of northeast Austalia. In: P.D. Crevello and e. al. (Editors),

Controls on Carbonate Platform and Basin DevelopmentSEPM, Tulsa, pp. 233-258.

Droxler, A.W., Alley, R.B., Howard, W.R., Poore, R.Z. and Burckle, L.H., 2003a. Unique and exceptionally long interglacial Marine Isotope Stage 11: window into Earth warm future climate. In: A.W. Droxler, P.R. Z. and B.L. H. (Editors), Earth's Climate and Orbital Eccentricity: The Marine Isotope Stage 11 Question. Geophysical Monograph 137. American Geophysical Union, Washington DC, pp. 1-14.

Droxler, A.W., Beaufort, L. and Labeyrie, L., 2002. Youthful Belize barrier reef: strenghtening the model for a mid-Bruhnes global establishment of modern barrier reefs. EOS Trans. AGU Fall Meet. Supp., Abstract PP71B-0391, 83(47).

Droxler, A.W. and Farrell, J.W., 2000. Marine Isotope Stage 11 (MIS 11): new insights for a warm future. Global and Planetary Change, 24(1): 1-5.

Droxler, A.W., Poore, R.Z. and Burckle, L.H. (Editors), 2003b. Earth's climate and orbital eccentricity: the Marine Isotope Stage 11 question. Geophysical Monograph, 137. American Geophysical Union, Washington DC, 240 pp.

Droxler, A.W. and Schlager, W., 1985. Glacial versus interglacial sedimentation-rates and turbidite frequency in the Bahamas. Geology, 13(11): 799-802.

Dunbar, G.B. and Dickens, G.R., 2003a. Late Quaternary shedding of shallow-marine carbonate along a tropical mixed siliciclastic-carbonate shelf: Great Barrier Reef, Australia. Sedimentology, 50(6): 1061-1077.

Dunbar, G.B. and Dickens, G.R., 2003b. Massive siliciclastic discharge to slopes of the Great Barrier Reef Platform during sea-level transgression: constraints from sediment cores between 15 degrees S and 16 degrees S latitude and possible explanations. Sedimentary Geology, 162(1-2): 141-158.

Dunbar, G.B., Dickens, G.R. and Carter, R.M., 2000. Sediment flux across the Great Barrier Reef Shelf to the Queensland Trough over the last 300 ky. Sedimentary Geology, 133(1-2): 49-92.

Eberli, G.P., Swart, P. K., Malone, M. J., et al., 1997. Proceedings ODP Initial Reports, 166. Ocean Drilling Program, College Station, TX.

Feary, D.A., Hine, A. C., Malone, M. J., et al., 2000. Proceedings ODP, Initial Reports 182 [Online].

Griffin, D.A., Middleton, J.H. and Bode, L., 1987. The tidal and longer period circulation of Capricornia, southern Great Barrier Reef. Austalian Journal of Marine and Freshwater Research, 38: 461-474.

Harris, P.T. et al., 2001. Continental shelf drift deposit indicates non-steady state Antarctic bottom water production in the Holocene. Marine Geology, 179(1-2): 1-8.

Harris, P.T., Domack, E., Manley, P.L., Gilbert, R. and Leventer, A., 1999. Andvord drift: A new type of inner shelf, glacial marine deposystem from the Antarctic Peninsula. Geology, 27(8): 683-686.

Hernandez-Molina, J. et al., 2003. Looking for clues to paleoceanographic imprints: A diagnosis of the Gulf of Cadiz contourite depositional systems. Geology, 31(1): 19-22.

Hine, A.C., Wilber, R.J., Bane, J.M., Neumann, A.C. and Lorenson, K.R., 1981. Offbank transport of carbonate sands along open, leeward bank margins - northern Bahamas. Marine Geology, 42(1-4): 327-348.

Hollister, C.D., Flood, R. and McCave, I.N., 1978. Plastering and decorating in North Atlantic. Oceanus, 21(1): 5-13.

Imbrie, J. et al., 1993. On the structure and origin of major glaciation cycles 2: the 100,000-year cycle. Paleoceanography, 8(6): 699-735.

International Consortium for Great Barrier Reef Drilling, 2001. New constraints on the origin of the Australian Great Barrier Reef: Results from an international project of deep coring. Geology, 29(6): 483-486.

Isern, A.R. and Anselmetti, F., 2001. The influence of carbonate platform morphology and sea level on fifth-order petrophysical cyclicity in slope and basin sediments adjacent to the Great Bahama Bank. Marine Geology, 177(3-4): 381-394.

Isern, A.R., Anselmetti, F. S., Blum, P., et al., 2002. Proceedings ODP, Initial Reports, 194 [Online].

Isern, A.R., McKenzie, J.A. and Feary, D.A., 1996. The role of sea-surface temperature as a control on carbonate platform development in the western Coral Sea. Palaeogeography Palaeoclimatology Palaeoecology, 124(3-4): 247-272.

James, N.P. and Mountjoy, E.W., 1983. Shelf-slope break in fossil carbonate platforms: an qverview. In: D.J. Stanley and G.T. Moore (Editors), The Shelfbreak: Critical Interface on Continental Margins. Special Publication 33. Society of Economic Paleontologists and Mineralogists, pp. 189-206.

Kershaw, A.P. and Nanson, G.C., 1993. The last full glacial cycle in the Australian region. Global and Planetary Change, 7(1-3): 1-9.

Kershaw, P., Moss, P. and Van der Kaars, S., 2003. Causes and consequences of long-term climatic variability on the Australian continent. Freshwater Biology, 48(7): 1274-1283.

Laskar, J., 1990. The chaotic motion of the solar system: a numerical estimate of the chaotic zones. Icarus, 88: 266-291.

Maxwell, W.G.H. and Swinchatt, J.P., 1970. Great Barrier Reef - regional variation in a terrigenous-carbonate province. Geological Society of America Bulletin, 81(3): 691-&.

Middleton, J.H. et al., 1994. Circulation and water mass characteristics of the southern Great Barrier Reef. Australian Journal of Marine and Freshwater Research, 45: 1-18.

Millwood, L.D., Hawkins Jr., D.L. and Wells, S.M., 2002. Data Report: Utilizing color reflectance analysis as a carbonate concentration proxy. In: C. Richter (Editor), Scientific Results Leg 181 [Online]. Proceedings ODP, pp. 1-50.

Mix, A.C., Harris, S.E. and Janecek, T.R., 1995. Estimating lithology from nonintrusive reflectance spectra. In: N.G. Pisias, L.A. Mayer, T.R. Janecek, A. Palmer-Julson and T.H. van Andel (Editors), Proceedings ODP, Scientific Results Leg 138Ocean Drilling Program.

Mudelsee, M. and Schulz, M., 1997. The Mid-Pleistocene climate transition: onset of 100 ka cycle lags ice volume build-up by 280 ka. Earth and Planetary Science Letters, 151(1-2): 117-123.

Mullins, H.T., Neumann, A.C., Wilber, R.J., Hine, A.C. and Chinburg, S.J., 1980. carbonate sediment drifts in northern Straits of Florida. AAPG Bulletin-American Association of Petroleum Geologists, 64(10): 1701-1717.

Multer, H.G., Gischler, E., Lundberg, J., Simmons, K.R. and Shinn, E.A., 2002. Key Largo Limestone revisited: Pleistocene shelf-edge facies, Florida Keys, USA. Facies, 46: 229-271.

Page, M.C., *in press*. Data report: variations in bulk carbonate content, Hole 1198A, 0-23 mbsf. In: A.R. Isern, F.S. Anselmetti and P. Blum (Editors), Proceedings ODP Scientific Results Leg 194Ocean Drilling Program, College Station, TX.

Page, M.C., Dickens, G.R. and Dunbar, G.B., 2003. Tropical view of Quaternary sequence stratigraphy: siliciclastic accumulation on slopes east of the Great Barrier Reef since the Last Glacial Maximum. Geology, 31(11): 1013-1016.

Paillard, D., Labeyrie, L. and Yiou, P., 1996. Macintosh program performs time-series analysis. EOS Trans., 77: 379.

Pigram, C.J., Davies, P.J., Feary, D.A. and Symonds, P.A., 1992. Absolute magnitude of the second-order middle to late Miocene sea-level fall, Marion Plateau, northeast Australia. Geology, 20: 858-862.

Posamentier, H.W., Allen, G.P., James, D.P. and Tesson, M., 1992. Forced regressions in a sequence stratigraphic framework - concepts, examples, and exploration significance. AAPG Bulletin-American Association of Petroleum Geologists, 76(11): 1687-1709.

Posamentier, H.W. and Vail, P.R., 1988. Sequences, systems tracts, and eustatic cycles. AAPG Bulletin-American Association of Petroleum Geologists, 72(2): 237-237.

Raymo, M.E. and Nisancioglu, K., 2003. The 41 kyr world: Milankovitch's other unsolved mystery. Paleoceanography, 18(1).

Read, J.F., 1982. Carbonate Platforms of passive (extensional) continental margins: types, characteristics, and evolution. Tectonophysics, 81: 195-212.

Shackleton, N.J., Berger, A. and Peltier, W.R., 1990. An alternative astronomical calibration of the lower Pleistocene timescale based on ODP Site 677. Transactions Royal Society of Earth Science, 81: 251-261.

Shackleton, N.J. and Hall, M.A., 1989. Stable Isotope history of the Pleistocene at ODP Site 677. In: K. Becker, H. Sakai and e. al. (Editors), Proceedings ODP Scientific Results 111. Ocean Drilling Program, College Station, TX, pp. 295-376.

Shipboard Scientific Party, 2002. Site 1198. In: A.R. Isern, F.S. Anselmetti, P. Blum and et al. (Editors), Proceedings ODP Initial Reports 194. pp. 1-75 [Online].

Swart, P.K. et al., 2002. Data report: carbonate mineralogy of sites drilled during Leg 182. In: A.C. Hine, D.A. Feary and M.J. Malone (Editors), Proceedings of the ODP Scientific Results Leg182,Ocean Drilling Program, College Station, TX, pp. 1-14.

Symonds, P.A., Davies, P.J. and Parasai, A., 1983. Structure and stratigraphy of the Great Barrier Reef. Bureau of Mineral Resources Journal of Geology and Geophysics, 8: 277-291.

Tucker, M.E. and Wright, V.P., 1990. Carbonate Sedimentology. Blackwell Scientific Publications, 482 pp.

Vail, P.R., Mitchum, R.M., Jr. and Tompson, S., 1977. Seismic stratigraphy and global changes of seal evel, Part 4: global cycles of relative changes of sea level. In: P.C. E. (Editor), Seismic Stratigraphy - Applications to Hydrocarbon Exploration Memoir 26. American Association of Petroleum Geologists, pp. 83 - 97.

Van Wagoner, J.C. et al., 1988. An overview of sequence stratigraphy and key definitions. In: C.K. Wilgus and e. al. (Editors), Sea-level Changes: An Integrated Approach 42. Society of Economic Paleontologists and Mineralogists, Tulsa, OK, pp. 39-40.

Webster, J.M. and Davies, P.J., 2003. Coral variation in two deep drill cores: significance for the Pleistocene development of the Great Barrier Reef. Sedimentary Geology, 159(1-2): 61-80.

Wilson, J.L., 1967. Cyclic and reciprocal sedimentation in Virgilian strata of southern New Mexico. Geological Society of America Bulletin, 78(7): 805-&.

Woolfe, K.J., Larcombe, P., Naish, T. and Purdon, R.G., 1998. Lowstand rivers need not incise the shelf: an example from the Great Barrier Reef, Australia, with implications for sequence stratigraphic models. Geology, 26(1): 75-78.